Published in final edited form as:
Nat Neurosci. 2013 December ; 16(12): 1802–1811. doi:10.1038/nn.3550.

Network state-dependent inhibition of identified hippocampal CA3 axo-axonic cells *in vivo*

Tim J Viney[#1], **Balint Lasztoczi**[#1,2], **Linda Katona**[#1], **Michael G Crump**[#1], **John J Tukker**[1], **Thomas Klausberger**[1,2], and **Peter Somogyi**[1,2]

[1]Medical Research Council Anatomical Neuropharmacology Unit, Department of Pharmacology, Oxford University, Oxford, UK

[2]Center for Brain Research, Medical University Vienna, Vienna, Austria

[#] These authors contributed equally to this work.

Abstract

Hippocampal sharp waves are population discharges initiated by an unknown mechanism in pyramidal cell networks of CA3. Axo-axonic cells (AACs) regulate action potential generation through GABAergic synapses on the axon initial segment. We found that CA3 AACs in anesthetized rats and AACs in freely moving rats stopped firing during sharp waves, when pyramidal cells fire most. AACs fired strongly and rhythmically around the peak of theta oscillations, when pyramidal cells fire at low probability. Distinguishing AACs from other parvalbumin-expressing interneurons by their lack of detectable SATB1 transcription factor immunoreactivity, we discovered a somatic GABAergic input originating from the medial septum that preferentially targets AACs. We recorded septo-hippocampal GABAergic cells that were activated during hippocampal sharp waves and projected to CA3. We hypothesize that inhibition of AACs, and the resulting subcellular redistribution of inhibition from the axon initial segment to other pyramidal cell domains, is a necessary condition for the emergence of sharp waves promoting memory consolidation.

During slow wave sleep (SWS), quiet wakefulness and consummatory behavior, large-amplitude, 30–120-ms-duration ‘sharp wave’ voltage deflections have been observed in extracellular recordings throughout the mammalian hippocampal formation[1], which occur simultaneously with 130–230 Hz ‘ripples’ most pronounced in stratum pyramidale (sPyr) of CA1 (refs. 2,3). These sharp wave–ripple complexes (SWRs) are required for memory

Correspondence should be addressed to T.J.V. (tim.viney@pharm.ox.ac.uk), B.L. (balint.lasztoczi@meduniwien.ac.at) or P.S. (peter.somogyi@pharm.ox.ac.uk).

AUTHOR CONTRIBUTIONS

T.J.V., B.L., L.K., M.G.C., J.J.T., T.K. and P.S. collected and analyzed data and wrote the paper. To expand on the equal-contributions footnote, each of the first four authors made important—though different—contributions, and hence they should be considered equal first authors.

Note: Any Supplementary Information and Source Data files are available in the online version of the paper.

COMPETING FINANCIAL INTERESTS

The authors declare no competing financial interests.

Europe PMC Funders Author Manuscripts

consolidation[4] and have been postulated to originate from groups of pyramidal neurons in CA3 participating in a synchronous 'population burst', which is transmitted to the downstream CA1 region via Schaffer collaterals[5]. A proposed mechanism for SWR initiation is through disinhibition of pyramidal cells via dynamic state-dependent interactions between GABAergic neurons and glutamatergic inputs[1]. Indeed, *in vivo* recordings show that some unidentified interneurons decrease and others increase their firing during SWRs[5,6]. Interneurons innervate different subcellular domains of pyramidal neurons, which in dorsal CA1 correlate with their firing patterns during, for example, SWRs[7]. Furthermore, cell type–specific spatiotemporal activity also depends on extrahippocampal inputs from structures such as the medial septum[8], raphe nuclei and entorhinal cortex[9]. Therefore, it is necessary to define the temporal contribution of distinct cell types that may influence or regulate SWR generation.

One group of hippocampal interneurons expresses the calcium-binding protein parvalbumin. Within this group in CA1, bistratified cells target pyramidal cell dendrites in stratum oriens (sOri) and stratum radiatum (sRad), basket cells target pyramidal cell somata and proximal dendrites, and AACs exclusively target the pyramidal cell axon initial segment (AIS). This latter, enigmatic GABAergic interneuron was discovered by János Szentágothai (1912–1994) as the chandelier cell in the neocortex[10], which he later called the axo-axonal cell when its synaptic target, the AIS, was identified[11]. In marked contrast to parvalbumin-expressing bistratified and basket cells, CA1 AACs do not fire during SWRs[12,13]. This may enable the recruitment of CA1 pyramidal cells during SWRs, as this cell type is ideally placed to regulate pyramidal cell firing. However, SWRs are generated in the upstream CA3 region[5], where the firing activity of AACs *in vivo* is unknown.

RESULTS

Identification of hippocampal AACs

To assess the contributions of AACs to the hippocampal network, we recorded the activity of single interneurons in both urethane-anesthetized and freely moving rats, followed by juxtacellular labeling (Fig. 1 and Supplementary Fig. 1). We identified nine AACs (from nine rats) on the basis of the presence of radial rows of boutons (cartridges) around the sPyr-sOri border (Fig. 1a,c)[14]. Dendrites of seven AACs crossed stratum lucidum (sLuc), demonstrating the cells' location in CA3. The dendrites were radially distributed across all strata, with a broad tuft aligned with the entorhinal cortical input in stratum lacunosum-moleculare (sLacMol) (n = 8 AACs, Fig. 1a), representing 34.7 ± 7.6% (mean ± s.d.) of the total dendritic length (n = 3 AACs, Fig. 1a,b). A smaller proportion was found in sRad (11.8 ± 8.3%) and only minor proportions in sLuc (1.9 ± 0.4%) and sPyr (4.9 ± 2.4%). The highest proportion of dendrites was in sOri and the alveus (46.7 ± 6.7%). Thus, CA3 AAC dendrites are aligned with pyramidal cell dendrites[15]. One CA3 AAC had dendrites and axon in CA2 (Fig. 2a). From two AACs recorded in freely moving rats, one was located in CA2 and had axon innervating both CA2 and CA3 but not CA1; the other was located in CA1 and innervated CA1 pyramidal cells.

Next we tested the molecular profiles, post-synaptic targets and firing patterns of AACs (Table 1). All AACs were immunoreactive for parvalbumin (PV^+) (n = 9 of 9 cells

examined), and their somatodendritic membrane expressed small puncta and large patches of ErbB4 (ref. 16) (n = 5 of 5 cells) (Fig. 1d,e). In contrast to other identified PV^+ cells, such as CA1 bistratified cells and oriens lacunosum-moleculare cells[12,13], AACs lacked detectable immunoreactivity for neuropeptide Y (NPY) and somatostatin (SOM) (n = 0 of 2 for both molecules) and were also immunonegative for neuronal calcium-binding protein 1 (NECAB1)[17] (n = 0 of 4 tested cells).

Testing for postsynaptic targets using ankyrin G, a marker for the AIS[18], showed that AAC boutons targeted the AISs of pyramidal cells[14] (n = 3 cells, Fig. 2b). These AISs were covered by vesicular GABA transporter (VGAT)-immunoreactive boutons, the labeled AAC terminals being a subset of these (Fig. 2b). Electron microscopy confirmed that these sites were GABAergic synapses[14] with membrane specialization (100% targeted AISs[19]; n = 7, 13, 11, 14, 10 and 9 synapses for cells B10a, LK24g, TV34n, B45a, B44a and B53b, respectively; Fig. 2c and Supplementary Figs. 1a and 2). Thus, CA3 AACs release GABA selectively on the AIS.

Firing patterns of AACs during sharp waves

To explore the firing patterns of CA3 AACs, we identified SWRs (90–200 Hz oscillations) and theta oscillations (3–6 Hz) in local field potentials (LFPs) recorded in both CA3 and CA1 of anesthetized rats (Figs. 1f,g and 2a). Transitions between different states occurred spontaneously or were promoted by administration of anesthetics (SWRs and non-theta states) or a tail pinch (theta). Coincident with the occurrence of SWRs, firing of AACs often ceased completely, despite firing heavily before and after (Fig. 1f). The number of action potentials fired by individual CA3 AACs was less during SWRs than expected from their firing in a ±10-s window around the SWRs (SWRs versus 'peri-SWRs' significant at α = 0.05 with Mann-Whitney U-test in 3 of 3 and 5 of 5 cells for CA3 and CA1 SWRs, respectively; Fig. 2e and Table 1). Mean (± s.d.) firing rates dropped from 24.6 ± 4.0 Hz and 22.8 ± 3.1 Hz peri-SWR to 4.4 ± 3.7 Hz and 4.8 ± 3.5 Hz during SWRs (P = 0.039 and 6×10^{-4}; t_2 = 4.9 and t_4 = 9.7; n = 3 cells and 5 cells, for SWRs detected in CA3 and CA1, respectively; paired Student's t-tests; Fig. 2e). We detected significant variation in the mean firing rate of AACs as a function of normalized SWR time ($P = 4 \times 10^{-8}$ and 6×10^{-13}; $F_{31,64}$ = 4.88 and $F_{31,128}$ = 5.74; n = 3 and 5 cells for CA3 and CA1 SWRs, respectively; one-way ANOVA), with a significant reduction in the rate associated with SWR occurrence (Tukey's *post hoc* multiple comparisons test; Fig. 2d). Consistent with the generation of SWRs in CA3 (ref. 5), we found that 30 ± 10% (mean ± s.d.) of detected SWRs occurred coincidentally in CA3 and downstream CA1 (n = 3 experiments from 3 rats). Some SWRs (27 ± 4.5%) detected by the CA3 electrode did not recruit the CA1 area at the CA1 electrode site; others detected only in CA1 (43 ± 14%) could have originated from sites other than that of the CA3 electrode. Suppression of CA3 AAC firing was similar irrespective of where the SWRs were detected (reduction to 19 ± 14% versus 21 ± 13% during SWRs in CA3 and CA1, n = 3 and 5 cells, respectively; P = 0.9; t_6 = 0.13; two-sample Student's t-test; Fig. 2e). In both areas, small increases in the power of 90–200 Hz oscillations, below the threshold of SWR detection and possibly reflecting distant, localized SWRs, were often associated with AAC silencing (Fig. 1f), suggesting that the suppression of AACs occurs on most SWRs.

To test whether the observed suppression of firing during SWRs could be detected in animals without anesthesia, we examined firing patterns of identified AACs recorded in drug-free, freely moving rats[20]. During SWS and quiet wakefulness, we observed a reduction in AAC firing during local SWRs (Fig. 2f and Supplementary Fig. 1b; 130–230 Hz oscillations). Identified AACs in both CA2 and CA1 significantly decreased their firing rate during SWRs compared to peri-SWR periods (CA2, cell LK24g: 0.72 Hz versus 8.8 Hz, $P = 6 \times 10^{-7}$, $n = 112$ SWRs; CA1, cell TV34n: 2.4 Hz versus 6.9 Hz, $P = 0.026$, $n = 61$ SWRs; Mann-Whitney *U*-test; Fig. 2d and Table 1). The overall firing rate was very low during resting states, when SWRs occurred (Supplementary Fig. 3 and Table 1). Occasionally, AACs fired in bursts (Fig. 2f) uncorrelated to SWRs. We conclude that AACs are inhibited during SWRs under drug-free conditions also.

Theta- and gamma-modulated firing of AACs

During theta oscillations under anesthesia, CA3 AACs fired rhythmically at 28.8 ± 4.2 Hz (mean ± s.d.; $n = 5$ cells from 5 rats), with six to eight action potentials per cycle (Fig. 1g and Table 1). Firing of AACs was lowest around theta troughs detected either locally in CA3 or in CA1 (Figs. 2a and 3a), suggesting a reduction in GABAergic input to CA3 AISs at this phase (Fig. 2b,c). Correspondingly, the preferred theta phase of firing was close to the peak, at 146° ± 28.1° for CA3 theta oscillations (circular mean ± circular s.d.; $n = 6$ cells; Fig. 3a and Table 1) and at 183° ± 21.7° for CA1 theta ($n = 5$ cells; only CA1 electrode in sPyr included; all AACs significant at $\alpha = 0.05$, Rayleigh test; Fig. 3a and Table 1). Consistent with the strong theta modulation of AACs, the mean vector lengths were similarly high (0.44 ± 0.07 in CA3 versus 0.45 ± 0.06 in CA1, mean ± s.d.; $P = 0.48$, $t_5 = 0.75$, $n = 6$, paired *t*-test). In freely moving rats, theta oscillations were observed during head movements and postural shifts; the animals remained in the same location throughout the recording period. Firing of AACs during movement occurred at a high rate and was rhythmic but intermittent (Fig. 3b,c, Supplementary Figs. 1c and 3a,b, and Table 1). Firing rates and consequent GABA release on CA2 and CA3 pyramidal cells (LK24g) and on CA1 pyramidal cells (TV34n) were lowest close to theta troughs, with preferred firing phases of 191° and 225°, respectively (phase distributions significantly different from uniform at $\alpha = 0.05$, Rayleigh tests; Fig. 3b and Table 1). Notably, AACs fired at a similar rate to CA1 PV^+ basket cells (PVBCs)[20] during theta oscillations in drug-free rats (Supplementary Fig. 3a,c) but were more strongly theta-modulated (AAC vector lengths: 0.48 in CA2, LK24g; 0.42 in CA1, TV34n; mean of mean vector lengths ± s.d. for 5 PVBCs[20], 0.22 ± 0.06). Differences in firing of AACs and PVBCs were evident across behavioral states (Supplementary Fig. 3b,d).

Identified CA3 AACs are not coupled to kainate-induced gamma oscillations *in vitro*[21], whereas CA1 AACs are coupled locally *in vivo*[22]. We have examined the relationship between AAC firing and 15–100 Hz LFP oscillations under anesthesia. We observed coupling (at $\alpha = 0.01$, Rayleigh test; $n = 33{,}003$, 30,870, 9,633, 14,673, 26,474 and 34,760 spikes for cells B10a, B45a, B53b, B62a, J54a and J67d, respectively) to CA1 gamma oscillations (mean vector length (reflecting phase coupling strength) $r = 0.06 \pm 0.04$ at the frequency of strongest coupling, 59 ± 12 Hz; mean ± s.d.; $n = 6$ cells; Fig. 3f) and relative to CA3 gamma oscillations (Fig. 3d–f) from either the local electrode ($r = 0.16 \pm 0.09$ at the

strongest coupling frequency, 71 ± 24 Hz; $n = 6$; $P = 0.066$, $t_5 = 2.35$; for r compared to CA1, paired t-test; Fig. 3f) or a nearby tetrode in CA3 sPyr ($n = 2$; Fig. 3d–f). Variability in firing phase may have resulted from the variable position of the electrode tips (compare Figs. 2a and 3f). Nevertheless, CA3 AACs show significant phase-coupling to gamma oscillations, comparable in strength and phase to those of CA3 pyramidal cells[23] and PVBCs[24].

Identification of inputs to AAC dendrites

Next we investigated synaptic inputs to AAC dendrites that could shape their firing patterns. Immunoreactivity for the presynaptic active-zone protein bassoon[25] showed that 9.7 ± 0.7% (mean ± s.d.) of putative synapses colocalized with VGAT puncta ($n = 215$ bassoon puncta, 3 cells from 3 rats; Fig. 4a), suggesting a relatively small proportion of GABAergic synapses on dendrites. Electron microscopy confirmed that AAC dendrites receive GABAergic synaptic input ($n = 22$ $VGAT^+$ terminals with synaptic junctions on dendrites of AAC B10a; Fig. 4b). These inputs could originate from the medial septum or from hippocampal interneurons. Two molecular markers differentiating the source of GABAergic terminals are parvalbumin and vasoactive intestinal polypeptide[26], but the AAC-dendrite-innervating $VGAT^+$ puncta were immunonegative for both molecules (data not shown).

Large mossy fiber terminals of dentate granule cells target pyramidal cell spines in sLuc, whereas thin filopodial extensions target interneuron dendrites[27]. Surprisingly, we have also found synapses from large mossy fiber terminals on identified AAC dendrites, which also targeted the thorny excrescences of pyramidal cells (Fig. 4c and Supplementary Fig. 4). Smaller boutons in sLuc, representing the filopodial extensions, also made synapses on AAC dendrites. From a total of 52 (cell B10a) and 82 (cell B45a) synaptic junctions sampled on 2 dendrites of each cell in sLuc, 6 and 3 synapses were made by large mossy fiber terminals, respectively. The metabotropic glutamate receptor type 7b (mGluR7b) is localized to the presynaptic active zone of mossy fiber terminals predominantly in synapses to interneurons[28]. However, mGluR7b-immunoreactive puncta were not found around AAC dendrites, in contrast to adjacent highly decorated unlabeled (neurobiotin-lacking) interneuron dendrites (Fig. 4d). These data show that AAC dendrites receive similar mGluR7b-negative glutamatergic granule cell input to that of pyramidal cells[29].

Immunonegativity for SATB1 identifies PV^+ AACs

Specific transcription factors mark neuronal subpopulations. We investigated the immunoreactivity for special AT-rich sequence binding protein 1 (SATB1; Fig. 5), which labels unidentified hippocampal interneurons[30]. We found SATB1 immunoreactivity in the nuclei of some PV^+ (Fig. 5a), NPY^+, SOM^+, $calbindin^+$, $procholecystokinin^+$ and $ErbB4^+$ interneurons, but not in neurons immunoreactive for neuronal nitric oxide synthase (data not shown). In both CA3 and CA1, some PV^+ neurons, among other, $SATB1^+PV^+$ double-positive neurons, lacked detectable immunoreactivity for SATB1 (were $SATB1^-$) (Fig. 5b,c).

Of PV^+ interneuron types with somata in or near sPyr—AACs, basket cells and bistratified cells[31]—only the bistratified cells express SOM and NPY[13]. We detected SATB1

immunoreactivity in all PV^+ neurons that were either SOM^+, NPY^+ or double-positive in sPyr of both CA3 (n = 25 of 25 cells; Fig. 5b) and CA1 (n = 46 of 46 cells). Of all PV^+ somata located in CA3 sPyr (n = 236 cells), 10.7 ± 4.4% (mean ± s.e.m. in 4 sections from 3 rats) were immunoreactive for both SATB1 and either SOM or NPY or both, 56.9 ± 7.7% were immunoreactive for SATB1 alone and 32.5 ± 7.6% showed immunoreactivity for neither SATB1 nor SOM or NPY (Fig. 5e). All PV^+ neurons were positive for the $GABA_A$ receptor α1 subunit[31] (Fig. 5b–d). Similar proportions of PV^+ somata were observed in CA1 (13.7 ± 4.2% $SATB1^+SOM^+$, $SATB1^+NPY^+$ or $SATB1^+SOM^+NPY^+$; 59.7 ± 3.3% $SATB1^+$ only; 26.5 ± 3.8% $SATB1^-$; n = 362 cells, 4 sections, 3 rats; Fig. 5e). The proportion of PV^+SATB1^+ neurons is consistent with previous counts of putative PVBCs[31]. We found similar proportions of PV^+ cells in mouse, suggesting that certain mouse PV^+ interneurons may be homologous to those characterized in the rat[32] (mouse CA3: 13.5 ± 3.6% $SATB1^+SOM^+$; 59.8 ± 3.4% $SATB1^+$ only; 26.7 ± 3.8% $SATB1^-$; n = 248 cells, 4 sections, 3 mice; CA1: 8.5 ± 4.3% $SATB1^+SOM^+$; 69.3 ± 5.2% $SATB1^+$ only; 22.2 ± 4.5% $SATB1^-$; n = 297 cells, 4 sections, 3 mice; Fig. 5e). Of note, we often observed clusters of neurons with a similar molecular profile, such as $PV^+SATB1^+SOM^-$ (Fig. 5d) or $PV^+SATB1^-SOM^-$, suggesting grouping of interneuron types.

To determine whether SATB1 immunoreactivity can be used to differentiate PVBCs from AACs, we tested identified interneurons labeled *in vivo* with neurobiotin. Five of five CA3 and one of one CA2 AACs lacked detectable nuclear SATB1 immunoreactivity (Figs. 1d and 5f and Table 1), as did two AACs from intermediate CA1 (TF31a, TF35c). Six of six identified PVBCs in CA1 were $SATB1^+$ (M01b, K03b and B102b; TV08k, K208c and O83f[20]; Fig. 5f), as was one PV^+SOM^+ bistratified cell in CA3 (TV32n). Thus, PV^+ interneurons that do not express SATB1 are AACs, representing ~30% of the PV^+ population in sPyr of both CA3 and CA1.

Innervation of AACs by the medial septum

Medial septal GABAergic neurons innervate diverse types of hippocampal interneurons[8]. We labeled the axons of medial septal neurons with *Phaseolus vulgaris* leucoagglutinin (PHA-L; n = 3 rats; Fig. 6a). In the medial septum, we observed clusters of labeled neurons, and axonal targets were consistent with known septal projections[33], including the hippocampus. In a control, PHA-L injected in the lateral septum produced very sparse labeling in the hippocampus.

Septo-hippocampal axons in CA3 and CA1 were of either type I (thick, putatively GABAergic) or type II (thin, putatively cholinergic)[8]. Individual type I axons had boutons apposed to the somata and proximal dendrites of some PV^+ neurons but they bypassed others, suggesting preferential targeting of distinct interneuron types (n = 41 PV^+ neurons innervated in CA3 and CA1, 36 axons; Fig. 6b). Some axons strongly innervated $SATB1^-PV^+$ neurons (putative AACs; n = 18 targeted cells in CA3, 17 axons) and bypassed adjacent $SATB1^+PV^+$ neurons (Fig. 6c). We also followed single septal axons that targeted other CA3 PV^+ interneurons but not putative AACs, and in one case observed two $SATB1^+PV^+$ neurons each with seven PHA-L boutons apposed to their somata in a ‘basket-like’ arrangement (Supplementary Fig. 5a,b). Similarly to those in CA3, $SATB1^-PV^+$

neurons in CA1 were targeted by axons (n = 6 cells, 6 axons) that did not innervate nearby SATB1$^+$PV$^+$ neurons (Supplementary Fig. 5d,e). We also immunolabeled CA1 pyramidal neurons using the marker SATB2 (ref. 34) but did not observe any septal axons in sPyr innervate these neurons in a basket-like manner around the somata (Supplementary Fig. 5d). These data suggest a medial septal input preferentially targeting AACs in both CA3 and CA1.

One population of GABAergic septo-hippocampal axons are immunoreactive for parvalbumin in rat[35]. We tested the axons targeting the SATB1$^-$PV$^+$ neurons for parvalbumin and VGAT[36] using confocal microscopy. Two out of ten axons targeting SATB1$^-$PV$^+$ somata were immunoreactive for parvalbumin, in seven axons parvalbumin was undetectable and in one axon we could not test immunoreactivity. Of the septal boutons apposed to SATB1$^-$PV$^+$ somata, 25.0% were PV$^+$ and in 57.7% parvalbumin was undetectable (17.3% were undetermined; n = 104 boutons; 10.4 ± 6.0 per soma observed in fluorescence; mean ± s.d.; Fig. 6c). Notably, five of ten axons targeting SATB1$^+$PV$^+$ neurons showed immunoreactivity for parvalbumin (undetectable in two, undetermined in three; Supplementary Fig. 5c). Most (72.9% of) septal boutons on SATB1$^+$PV$^+$ somata were PV$^+$ (undetectable in 10.4% and undetermined in 16.6%; n = 48 boutons; 4.8 ± 3.2 per soma; Supplementary Fig. 5c). Therefore, compared to other PV$^+$ interneurons using immunofluorescence, putative AACs (SATB1$^-$PV$^+$ neurons) appeared to be mainly innervated by septal afferents with undetectable levels of parvalbumin. We observed both strongly and weakly parvalbumin-immunoreactive somata in the medial septum (data not shown).

To test the neurotransmitter in soma-innervating septal terminals, we analyzed VGAT-immunoreactivity around PV$^+$ neurons. We observed, for example, a SATB1$^-$ soma but not an adjacent SATB1$^+$ soma innervated by PHA-L$^+$ boutons, which contained VGAT puncta (Fig. 6d). GABAergic synapses are rich in the postsynaptic scaffolding protein gephyrin that regulates clustering of $GABA_A$ receptors[37]. Gephyrin-immunoreactive puncta on SATB1$^-$PV$^+$ neurons were aligned with PHA-L$^+$ boutons (Fig. 6e). Finally, we asked whether all apposed septal boutons established synapses with the SATB1$^-$PV$^+$ neurons. We identified PHA-L-labeled boutons in apparent contact with putative AAC somata in the light microscope (Supplementary Fig. 6). Boutons were electron microscopically sampled from three SATB1$^-$PV$^+$ cells (n = 15 of 39 boutons for a cell in CA3, Supplementary Fig. 6a–e; n = 13 of 29 boutons for another cell in CA3; n = 11 of 11 boutons for a cell in CA1), and all were apposed to the plasma membrane of the target cell. Synaptic junctions were found between 11 of 15, 12 of 13 and 10 of 11 boutons and the somata or dendrites (Supplementary Fig. 6f–j), some with multiple active zones. In the remaining boutons, the presence of synapses could not be tested owing to an oblique cutting angle. In no case did the boutons innervate any other cells; they made synapses only with the putative AAC. We conclude that all medial septal boutons made synapses with the target AACs, confirming the prediction derived from the gephyrin-immunoreactive puncta (Fig. 6e). Therefore, a subpopulation of GABAergic septo-hippocampal axons targets SATB1$^-$PV$^+$ but not SATB1$^+$PV$^+$ somata.

Septo-hippocampal neurons activated during sharp waves

Some medial septal cells increase their firing during hippocampal SWRs but whether they project to the hippocampus is unknown[38,39]. We asked whether any GABAergic septo-hippocampal neurons were activated during sharp waves. We extracellularly recorded and juxtacellularly labeled single medial septal neurons in anesthetized rats (Fig. 7). From 31 theta-modulated cells (at $\alpha = 0.05$ with Rayleigh test) that were recorded during >20 SWR events, 12 (38.7%; recorded from 11 rats) showed a variable and significant increase in firing during SWRs (at $\alpha = 0.05$ with Mann Whitney *U*-tests), on average from 12.0 ± 9.9 Hz peri-SWR to 28.5 ± 15.6 Hz (mean ± s.d.; Fig. 7c,e and Supplementary Table 1). In some cases, the SWR-activated cells fired rhythmically during non-theta periods[40] (not analyzed here), and we also observed activation during events that remained below the threshold for SWR detection with our criteria at the CA1 recording site (Fig. 7c). Five of the 12 cells could be labeled and identified, with 5 of 5 and 4 of 4 immunopositive for parvalbumin and hyperpolarization-activated cyclic nucleotide-gated potassium channel 4 (HCN4), respectively (Fig. 7a, Supplementary Fig. 5f,g and Supplementary Table 1). We note that parvalbumin immunoreactivity in the septum does not necessarily imply parvalbumin immunoreactivity in axonal boutons in distant target areas. Notably, 4 of 4 cells were also immunoreactive for SATB1. Of four cells, which were well labeled, two had axons in the fimbria with collaterals entering CA3 (ref. 35) (Fig. 7b and Supplementary Table 1), but their targets could not be identified. The other two cells had axons in the dorsal fornix and may have projected to the cortex; one of these cells had additional minor branches that entered medial CA1 and subiculum. Septal neurons (3 of 3 tested; Supplementary Table 1) were $VGAT^+$ in their local medial septal terminals (Fig. 7d) and were thus GABAergic.

All 12 cells that showed increased firing during SWRs were strongly phase-locked to different phases of theta oscillations (vector lengths of 0.46–0.76; Supplementary Fig. 5h,i and Supplementary Table 1)[39]. Interestingly, the two CA3-projecting cells fired in a counter-phase manner to the firing of hippocampal AACs (Fig. 3a), preferentially at the trough of CA1 theta oscillations (Supplementary Fig. 5h,i and Supplementary Table 1). We have demonstrated that some septo-hippocampal cells, potentially the sources of AAC innervation, fire in a pattern complementary to AACs during both SWRs and theta oscillations. However, on the basis of differences in levels of parvalbumin immunoreactivity in PHA-L-labeled septohippocampal terminals targeting $SATB1^-PV^+$ somata and the different firing patterns of septal cells, inhibition of AACs may be mediated by more than one medial septal cell type.

DISCUSSION

We have demonstrated that the firing of CA3 AACs is suppressed during sharp waves *in vivo*, resulting in a temporally and spatially restricted reduction of GABA release on the AISs of CA3 pyramidal cells. This is consistent with a key role of AACs in coordinating cell assembly reactivation by allowing excitatory interactions in the CA3 recurrent system selectively during sharp waves[5]. We propose that the inhibition of AACs causes a

subcellular redistribution of inhibition from the AIS to the soma and dendrites of pyramidal cells, creating conditions permissive for sharp wave initiation.

We show that the somata of AACs are innervated by a subset of GABAergic medial septal cells that do not target nearby $SATB1^{+}PV^{+}$ hippocampal neurons and that AACs also receive some dendritic inhibition[14]. Although we recorded SWR-activated septal cells that were immunopositive for parvalbumin, levels of this marker in PHA-L-labeled septal terminals targeting AACs varied. Subsets of septal GABAergic cells[38,39] that project to CA3 fired strongly around the trough of theta oscillations and could innervate AACs. Silencing AACs leads to rhythmic disinhibition of pyramidal cell AISs every 90–200 ms, which could contribute to the theta dipole across hippocampal strata[9,41], resulting in the population of pyramidal cells firing with highest probably at theta trough[23], the minimal firing phase of AACs. These interneurons may also receive recurrent CA3 pyramidal input[42] and entorhinal cortical input to their tufted dendrites in sLacMol, as well as two kinds of mGluR7b-lacking mossy fiber synaptic inputs to dendrites in sLuc, all contributing to their modulation by gamma oscillations.

When the animal becomes quiescent or enters SWS, cholinergic septal input and entorhinal and dentate glutamatergic input change CA3 network excitability in concert with interneurons, and the somatic GABAergic septal input to AACs would possess a different temporal structure than during theta oscillations. Our finding that the suppression of AAC firing during sharp waves occurs irrespective of its local origin at the electrode suggests that a selective and divergent inhibitory input, such as from the septum, silences most AACs. The AACs are synchronized also by means of gap-junction coupling[31]. During the sharp wave, within a 30–120-ms window, AACs may be strongly inhibited by this septal input and probably by other sources of GABA such as local interneurons[14], which may selectively shunt dendritic glutamatergic inputs to AACs. This in turn leads to a withdrawal of GABA from the AIS of pyramidal cells. Disinhibition of the AIS opens a short time window for pyramidal cells to fire at high probability and build up recurrent excitation[43], which enables sharp waves to occur[1] and time-compressed spike sequences to reemerge[44]. Under some *in vitro* conditions, GABA released on the AIS by AACs in the neocortex has been found to be excitatory[45,46]. Our finding that CA3 AACs fire at high frequencies with a temporal pattern inversely related to their postsynaptic targets, confirming previous results in CA1 (ref. 12), suggests that most pyramidal cell spikes are not driven by AACs and most AAC spikes inhibit rather than excite pyramidal cells[46,47], as originally suggested[11].

In contrast to AACs, PVBCs are activated during sharp waves and rhythmically release GABA to the somata and proximal dendrites of pyramidal cells every 4–8 ms. Because CA3 (ref. 24) and CA1 (refs. 12,32) PVBCs are phase locked to local ripple cycles, this cell type, along with strongly activated bistratified cells targeting dendrites[13], may be responsible for generating the fast oscillatory component of SWR events and temporally organizing the pyramidal cell assemblies[5,48].

Both CA3 AACs and PVBCs[24] have access to the same afferents as do pyramidal cells (in contrast to those in CA1; ref. 12), but their strikingly different firing patterns during sharp waves suggests different GABAergic input, matched by their differential expression of

SATB1. Indeed, these two cell types have been shown to have divergent network contributions *in vitro*[21]. Future studies in mice may shed light on the functional consequences of altering the relative GABAergic input specifically to these cell types and on the impact of AACs on sharp-wave initiation. Optogenetic studies exploring the causal relationship between firing of septal cells and AACs would require the establishment of specific markers for septal cell types that target AACs. As SATB1 is expressed by some septo-hippocampal neurons in rats and is also found in the mouse medial septum[30], recording from similar neurons in both wild-type and SATB1 mutant mice[49,50] might provide clues as to how they influence sharp wave generation. To our knowledge, SATB1 represents the first molecular marker that differentiates AACs and PVBCs in the hippocampus, and the septal input represents the first evidence of an identified source of GABAergic input to a single type of hippocampal interneuron. The firing increase of PVBCs and decrease of AACs at the onset of SWRs causes a subcellular redistribution of inhibition in pyramidal cells. According to this concept, AACs, acting as 'gatekeepers', select and control the firing of CA3 pyramidal cell assemblies during the replay of memory sequences.

ONLINE METHODS

In vivo recording, labeling, electrophysiological and statistical analyses

All procedures involving experimental animals were under approved personal and project licenses in accordance with the Animals (Scientific Procedures) Act, 1986 (UK) and associated regulations. Methods have been described in detail elsewhere[23]. Briefly, 250–350-g adult male Sprague-Dawley rats (housed with littermates on a normal light-dark cycle, lights on 08:00 to 20:00, 19–21 °C, 55% humidity) were anesthetized by urethane (1.25 g kg^{-1}, intraperitoneally), with supplemental doses of ketamine and xylazine (20 and 2 mg kg^{-1}, intraperitoneally; except for rat B62, which was given 5 and 2 mg kg^{-1}) as necessary. LFPs (0.3–300 Hz; 1 kHz sampling) were recorded by a glass electrode aimed at CA1 sPyr (4 mm posterior and 2 mm right from bregma, 10° postero-anterior angle, ~2.3 mm deep). LFPs and action potentials (0.8–5 kHz; 20 kHz sampling) of individual neurons were recorded by a glass electrode in CA3 (2.8 mm posterior and 2.8–3.8 mm right from bregma, 10° antero-posterior angle) or medial septum (0.6 mm anterior and 1.4 mm left from bregma, 15° latero-medial angle). The recorded cell was subsequently juxtacellularly labeled[51] with 1.5% neurobiotin (3% for medial septal cells) in 0.5 M NaCl. A recovery time of 4–10 h was used for medial septal cells. In some experiments, additional recordings were made by a tetrode pair inserted into CA3 sPyr[23]. For experiments in freely moving rats, methods have been previously described[20]. Adult rats LK24 and TV34 weighed 450 g and 477 g, respectively, at the time of headstage implantation. They were housed on a reverse light-dark cycle with the same temperature and humidity as described above. Buprenorphine (Vetergesic, 0.03 mg kg^{-1}, subcutaneously) was used peri-operatively for headstage implantation and craniotomy and duratomy procedures. Recordings began at least 24 h after the craniotomy over CA1–CA3, and a 3% neurobiotin solution in 0.5 M NaCl was used for juxtacellular labeling.

Analyses were performed in Spike2 (CED, Cambridge, UK) and MATLAB. We identified SWRs in anesthetized rats on the basis of the 90–200 Hz root-mean-square amplitude exceeding a threshold (5 s.d.; except J54a, for which the CA1 electrode was in sRad and we used 4 s.d. to improve detection). We detected SWRs in CA1 (6 experiments) or, when possible, in CA3 (3 experiments; CA3 glass electrode in B62 and J67, and one of the tetrode wires in B45). In freely moving rats, we used 130–230 Hz filtering[20], 4 s.d. threshold from the glass electrode. Theta and non-theta periods were identified in anesthetized rats on the basis of a theta (3–6 Hz) to delta (2–3 Hz) power ratio in the CA1 (or CA3 in J67) electrode of >4 (theta) or <2 (non-theta; SWRs were excluded) for at least 6 s. In freely moving rats, we used a 5–12 Hz theta to 2–4 Hz delta ratio[20]. The identified periods were taken as samples and firing rate comparisons were made by the Mann-Whitney *U*-test.

Theta phase was calculated by linear interpolation between troughs (designated 0° and 360°) identified in 3–6 Hz band-pass filtered traces for anesthetized experiments. For uniformity of circular phase distributions, we used the Rayleigh test[23], taking the mean phase and mean vector length as descriptive statistics for phase preference and coupling strength, respectively. Cell J54a was excluded from mean CA1 theta phase calculations because the CA1 electrode was in sRad instead of sPyr. Cell B53b was excluded from mean firing rate calculations because of unusually deep anesthesia.

To identify effects of SWRs on firing rates, the distribution of the numbers of action potentials during SWRs were compared to the distribution in identical time windows randomly placed 100 times in the ±10-s vicinity of the SWR (with other SWRs excluded; peri-SWR data)[23]. Distributions were compared by a Mann-Whitney *U*-test. We also analyzed temporal dynamics of firing during SWRs and created rate histograms as a function of normalized time, as previously described[12,23], averaged across different cells and statistically assessed with a one-way ANOVA. Individual bins were considered significant when a *post hoc* Tukey test disclosed a significant difference to at least one of the baseline bins (the first 12 bins of the histogram). The recording of B53b only had 7 SWRs so was not included in further statistical analyses, but its firing was qualitatively consistent with the other AACs.

Coupling to gamma oscillations was analyzed by calculating circular means of spike phase spectra (15–100 Hz; extracted with wavelet transformation), as previously described[23]. Spectra for all spikes but those during SWRs were included. For the local (CA3) glass electrode LFP, “spike artifacts” were substituted by linearly interpolated values.

No statistical methods were used to predetermine sample sizes but our sample sizes are similar to those reported in previous publications[12,20,23]. For some statistical tests used in this study data distribution was assumed to be normal (or von Mieses for circular data) but this was not formally tested.

Anterograde tracing

A 2.5% w/v solution of PHA-L (L-1110, Vector Laboratories)[52] in 0.1 M phosphate buffer (PB) was injected into the medial septum of 3 rats under isoflurane anesthesia. Coordinates from bregma: 0.6 mm anterior, 1.4 mm left, with a 15° latero-medial angle. Iontophoresis

was used to deliver PHA-L (5 μA positive current, 7 s duty cycle, 10–30 min delivery times) at 3 slightly different locations (6.5, 5.8, 5.5 mm depth from the brain surface for one rat; 6.2, 5.8, 5.5 mm for the other two rats). The electrode was placed at the first location for 15 min before stimulation and not moved until 5 min after each injection. Electrode tip diameter was ~10 μm. Following recovery, animals were kept for 4–18 days until perfusion. To assess the spatial extent of PHA-L delivery from within the septum, a fourth rat was injected in the lateral septum (6.2, 5.8, 5.5 mm depth, 10 min delivery times).

Tissue processing

After transcardial perfusion (4% paraformaldehyde, 15% v/v saturated picric acid and 0.05% glutaraldehyde in 0.1 M PB), brains were stored in 0.1 M PB with 0.05% sodium azide (PB-Az) at 4 °C. Coronal sections (70 μm; Leica VT 1000S vibratome) were washed three times in 0.1 M PB and stored in PB-Az at 4 °C. To find neurobiotin-labeled neurons, sections were either permeabilized in Tris-buffered saline (TBS) with 0.1% Triton X-100 (Tx) or subjected to one or two rounds of freeze-thaw over liquid nitrogen after cryoprotecting in 20% sucrose. After three or four washes in 0.1 M PB, sections were incubated in 1:1,000 streptavidin-conjugated Alexa Fluor 488 (Invitrogen) in TBS or TBS-Tx for 4 h at room temperature (RT) or overnight at 4 °C. After three washes, sections were mounted on slides in VectaShield (Vector Laboratories). For analysis, electron microscopy and reconstruction, sections were processed with the horseradish peroxidase (HRP) reaction to reveal neurobiotin with a diaminobenzidine (DAB) reaction product. Sections were incubated in 1:100 avidin–biotinylated peroxidase complex (ABC; Vectastain ABC Elite kit, Vector Laboratories) in TBS-Tx or TBS for 2–3 d at 4 °C. If sections were previously incubated in streptavidin, sections were additionally incubated with the biotinylated peroxidase complex for 4 h at RT or overnight at 4 °C before incubating in ABC. After three washes in 0.1 M PB, sections were incubated in a 0.5 mg/ml DAB (Sigma-Aldrich) solution containing glucose, ammonium chloride and 0–4% nickel ammonium sulfate. After 15 min, 0.2% glucose oxidase was added to generate H_2O_2 for the oxidation of DAB by peroxidase, forming a blue-black precipitate in the presence of nickel. After 40–60 min, depending on the darkness of the reaction product, sections were washed four times in 0.1 M PB. Next, sections were incubated in 0.2–1% osmium tetroxide in 0.1 M PB for 1 h and washed three times in 0.1 M PB. Sections were dehydrated in successive rounds of ethanol (50%, 70%, 90%, 95%, 100%), followed by propylene oxide (VWR International). Between the 70% and 90% ethanol washes, sections were incubated for 40 min in 2% uranyl acetate in 70% ethanol to enhance contrast for electron microscopy (see below). Next, sections were submerged in epoxy resin (Durcupan ACM Fluka, Sigma-Aldrich) and left overnight. Finally, sections were mounted on slides under a coverslip and the resin was polymerized at 60 °C for >24 h.

Immunohistochemistry

For sections subjected to freeze-thaw, TBS was used for all base solutions and washes. Otherwise, TBS-Tx was used throughout. Sections were blocked for 1 h in 10% normal horse serum (NHS) before application of a primary antibody solution containing 1% NHS for 3 d at 4 °C. Negative controls lacked the primary antibodies. See Supplementary Table 2 for specificity information and dilutions. After incubation, sections were washed three times

for 10 min each and then incubated in secondary antibody solution containing 1% NHS. The following secondary antibodies were used: donkey anti-rabbit Alexa Fluor 405 (1:250, Invitrogen; A31556 lot 55310A); donkey anti-mouse, anti-goat or anti–guinea pig DyLight405 (1:250, Jackson ImmunoResearch Laboratories; 715-475-151 lot 98883, 705-475-147 lot 96706, 706-475-148 lot 99779, respectively); donkey anti-rabbit or anti-goat Alexa Fluor 488 (1:1,000, Invitrogen; A21206 lot 556439, A11055 lot 49732A, respectively); donkey anti-rabbit, anti-goat, anti-sheep, anti-mouse or anti–guinea pig Cy3 (1:400, Jackson; 711-165-152 lot 98888, 705-165-147 lot 81185, 713-165-147 lot 87933, 715-165-151 lot 94510, 706-165-148 lot 86928, respectively); donkey anti-rabbit, anti-goat, anti-sheep, anti-mouse or anti–guinea pig Cy5 (1:250, Jackson; 711-175-152 lot 80443, 705-175-147 lot 72031, 713-175-147 lot 72156, 715-175-151 lot 88814, 706-175-148 lot 72155, respectively); donkey anti-rabbit, anti-goat or anti-mouse DyLight 649 (1:250, Jackson; 711-495-152 lot 98016, 705-495-147 lot 97534, 715-495-151 lot 94507, respectively), donkey anti-sheep or anti–guinea pig Alexa Fluor 647 (1:250, Jackson; 713-605-147 lot 102770, 706-605-148 lot 100905, respectively); donkey anti–guinea pig HRP (1:100, Jackson); and swine anti-rabbit HRP (1:100, Dako, Glostrup, Denmark; P0217). After 4 h at room temperature or 4 °C overnight, sections for immunofluorescence were washed three times for 10 min each and mounted on glass slides in VectaShield. For two-color DAB-based HRP enzyme reactions (rabbit anti-VGAT and neurobiotin), freeze-thawed sections were incubated in primary antibody as above, processed with ABC and then processed with DAB (without Ni^{2+}) and glucose oxidase to react the neurobiotin-labeled cell. Next sections were washed four times in 0.1 M PB and incubated overnight in anti-rabbit HRP secondary antibody solution. Sections were processed for DAB but using H_2O_2 as the substrate directly for 2–7 min. Processing continued as above. In experiments that used the biotinylated anti–PHA-L primary antibody, streptavidin Alexa Fluor 488 was used for fluorescence visualization followed by conversion with DAB as above (4% nickel ammonium sulfate).

Confocal imaging

An LSM710 confocal microscope (Axio Imager.Z1, Carl Zeiss) with ZEN 2008 software v5.0 (Zeiss) was used to acquire multichannel fluorescence images. DIC M27 Plan-Apochromat 63×/1.4 n.a. and alpha Plan-Apochromat 100×/1.46 n.a. oil immersion objectives were used with the following channels (laser and excitation wavelength, fluorophores, beam splitters, emission spectral filter): 405-30 solid state 405 nm with attenuation filter ND04, DyLight405, MBS-405, 409–499 nm; argon 488 nm, Alexa Fluor 488, MBS-488, 493–542 nm; HeNe 543 nm, Cy3, MBS-458/543, 552–639 nm; HeNe 633 nm, Cy5/DyLight 649/Alexa Fluor 647, MBS 488/543/633, 637–757 nm. Channels were acquired sequentially with an eight-bit dynamic range, and the pinhole size was set at 1 Airy unit for the shortest wavelength used; the pinhole sizes of the other channels were adjusted to values <1 Airy unit, giving all channels the same optical slice thickness. With the 63× lens and the 405-30 laser, the optical slice thickness was typically 0.6 μm. Using the argon laser as the shortest excitation wavelength, 1 Airy unit gave an optical slice thickness of 0.7 μm. Pixel number was calculated with Nyquist sampling, optimized for the channel having the shortest wavelength. At 63× with the 405-30 laser, sampling resolution was typically 12.686 pixel μm^{-1}, 0.08 × 0.08 × 0.43 μm voxels. At 100×, sampling was 13.173 pixel

μm^{-1}. We used the 63× lens for the majority of 3D images due to higher transmission, including for montages (zoomed out by 0.8). Assignment of antibody fluorophores was based on minimizing spectral overlap between channels. Synaptic markers were assigned the highest resolution channel. In some cases where markers showed no spatial overlap, two markers were sometimes labeled with the same fluorophore, increasing the number of markers used within one section: for example, gephyrin DyLight405 (post-synaptic puncta); SATB2 and PHA-L AF488 (nuclei and axons); SATB1 and NPY Cy3 (nuclei and Golgi apparatus); and parvalbumin DyLight649 (cytoplasm). Images were analyzed in ImageJ. Deconvolution (ZEN 2008) was used before quantifying bassoon puncta.

Quantification of immunolabeled neurons

To quantify SATB1 immunoreactivity in PV$^+$ neurons, cells in dorsal CA1 and CA3 of 70-μm-thick sections (from both adult rats and C57/BL6 mice) were counted using widefield epifluorescence on a Leitz DMRB microscope (Leica) equipped with PL Fluotar objectives. We counted only cells that had whole somata within sPyr, with the condition that the nucleolus must be visible in the fluorescence channel corresponding to parvalbumin. Cells were marked SATB1-immunonegative only when the mean pixel intensity of the nuclear region was the same as a background region of interest in the SATB1 channel. To confirm immunopositivity or immunonegativity, counted cells were sometimes scanned with the confocal microscope.

To quantify parvalbumin immunoreactivity in PHA-L-labeled septal axon terminals in the hippocampus, confocal microscopic *z*-stacks were analyzed. As a positive control, reference PHA-L-labeled axons immunopositive for parvalbumin were located at different depths in the *z*-stack of each brain section. Axons deep in the stack were excluded because of the lower signal-to-noise ratio. “Immunopositive” was defined as positive pixels in the axon or in axon boutons, similar to those in the positive control, compared to the background. “Undetectable” defines the limit of our method; we cannot rule out low parvalbumin immunoreactivity. “Undetermined” corresponds to PHA-L-labeled axons or axon boutons that were obscured by the parvalbumin immunoreactivity of larger structures.

Electron microscopy

Target areas (for example, axon-rich regions, or dendrites in sLuc) were cut from the resin-embedded 70-μm-thick sections and reembedded for ultramicrotome sectioning. Serial electron microscopic sections were cut and mounted on single-slot, pioloform-coated copper grids. A Philips CM100 transmission electron microscope fitted with a Gatan UltraScan 1000 CCD camera was used to acquire images. All boutons cut by the section plane were followed in serial sections and searched for synaptic junctions. AISs were identified as previously described[11]. All synapses found innervated AISs; none of the boutons could be shown to make a synapse with a dendrite or a soma. As the AISs are relatively small in diameter and may have tortuous courses, the membrane of boutons and the apposed AIS membrane is cut at an oblique angle in many cases, which makes it impossible to reveal the synaptic cleft even with tilting the sections in the electron microscope. Such cases were not counted. Initial identification of axon cartridges[14] at the light microscopic level (and their association with AISs using ankyrin G immunoreactivity) correlated with the electron

microscopic results. Mossy fibers were scanned in the vicinity of AAC dendrites in sLuc. Only clearly identified synapses were quantified. Nonlinear contrast adjustment was applied to all images.

Digital reconstruction and quantification

The full dendritic trees of three AACs were reconstructed in 3D from the series of nominally 70-μm-thick coronal sections. Dendrites were traced using Neurolucida (v.9, MBF Bioscience) on a Nikon Eclipse 80i microscope equipped with a Lucivid and a 100× 1.4 n.a. oil immersion Plan Apo VC objective lens. Laminar boundaries were drawn for all sections in Neurolucida and crossing points for all dendrites were checked individually and recorded. The outline of each section was also traced as a general reference for rotational alignment and confirmation of shrinkage correction. To aid the delineation of laminar and areal boundaries, immunoreactivity to mGluR2/3 (for sRad–sLacMol and sLuc–sRad)[28] and calbindin (for sLuc–sRad and CA3–CA2)[53] was sometimes tested on the sections with immunofluorescence and in immunoperoxidase reactions.

Because of tissue shrinkage, each section was expanded to its original unprocessed dimensions by applying shrinkage correction ratios, whenever possible using individual section values. In order to compensate for *z*-axis shrinkage, the section thickness was measured by visualizing the top and bottom surfaces of the tissue using DAPI staining, a Colibri 405-nm LED and the Axio Imager. Z1 microscope with the 100× 1.46 n.a. oil immersion objective lens. The mean thickness was calculated for each section from at least five *z* measurements taken along CA1, CA3 and dentate gyrus. Postprocessing (epoxy resin–embedded) section thickness was measured in Neurolucida. In some cases, the correction was done using the mean preprocessing thickness calculated from nondendritic sections. The same methods were applied for the lateral dimensions from images taken before and after processing.

Dendrites of B45a, B10a, J54a spanned 11, 11 and 9 consecutive sections, respectively. For B45a, freeze-thawed and Triton-treated dendritic sections had mean *z* dimension shrinkage correction ratios of 1.31 ± 0.07 (s.d.) and 1.40 ± 0.1, respectively. For *x*-*y* dimensions, the mean ratio for the freeze-thawed dendritic sections was 1.06 ± 0.02; dimensions of Triton-treated dendritic sections were scaled manually in Neurolucida to match the other corrected sections. For B10a, the mean shrinkage correction ratios were 1.07 ± 0.17 (freeze-thawed dendritic sections) and 1.27 ± 0.15 (Triton-treated dendritic sections) for the *z* dimension. For *x*-*y* dimensions, mean ratios were 1.05 ± 0.02 (freeze-thawed) and 1.08 ± 0.01 (Triton-treated); four dendritic sections were scaled manually. For J54a, the mean shrinkage correction ratios were 1.13 ± 0.11 (freeze-thawed) and 1.20 ± 0.14 (Triton-treated) for the *z* dimension. For *x*-*y* dimensions, the mean shrinkage correction ratios were 1.04 ± 0.02 (freeze-thawed) and 1.12 ± 0.03 (Triton-treated).

The total dendritic length per stratum in the shrinkage-corrected and spliced reconstructions was calculated using Neurolucida Explorer. For figures, reconstructions were rotated to obtain a semi-coronal projection, providing the maximum overlap between corresponding laminar boundaries from consecutive sections. A representative part of the B45a axon,

initially drawn on paper with a drawing tube, was photographed and superimposed onto the reconstructed dendrites.

Supplementary Material

Refer to Web version on PubMed Central for supplementary material.

ACKNOWLEDGMENTS

This paper celebrates the contributions of János Szentágothai (1912–1994) to neuroscience. We thank the excellent assistance of K. Detzner, D. Kotzadimitriou, B. Micklem and S. Biro. We thank J. Somogyi for advice on confocal microscopy and T. Forro, K. Hartwich and O. Valenti for the use of identified interneurons that they labeled *in vivo*. We are grateful to R. Shigemoto (National Institute for Physiological Sciences, Okazaki, Japan) and M. Watanabe (Department of Anatomy, Hokkaido University Graduate School of Medicine) for the gift of antibodies. We thank T. Ellender and P. Magill for comments on an earlier version of the manuscript. B.L. was supported by the Blaschko European Visiting Research Fellowship at Oxford; we acknowledge grant 242689 of the European Research Council, grant SCIC03 of the Vienna Science and Technology Fund and the Medical Research Council.

References

1. Buzsáki G. Hippocampal sharp waves — their origin and significance. Brain Res. 1986; 398:242–252. [PubMed: 3026567]
2. O'Keefe, J.; Nadel, L. The Hippocampus as a Cognitive Map. Oxford Univ. Press; 1978.
3. Buzsáki G, Horvath Z, Urioste R, Hetke J, Wise K. High-frequency network oscillation in the hippocampus. Science. 1992; 256:1025–1027. [PubMed: 1589772]
4. Girardeau G, Benchenane K, Wiener SI, Buzsáki G, Zugaro MB. Selective suppression of hippocampal ripples impairs spatial memory. Nat. Neurosci. 2009; 12:1222–1223. [PubMed: 19749750]
5. Csicsvari J, Hirase H, Mamiya A, Buzsáki G. Ensemble patterns of hippocampal CA3-CA1 neurons during sharp wave-associated population events. Neuron. 2000; 28:585–594. [PubMed: 11144366]
6. Csicsvari J, Hirase H, Czurko A, Mamiya A, Buzsáki G. Oscillatory coupling of hippocampal pyramidal cells and interneurons in the behaving rat. J. Neurosci. 1999; 19:274–287. [PubMed: 9870957]
7. Somogyi, P. Hippocampus: intrinsic organization. In: Shepherd, GM.; Grillner, S., editors. Handbook of Brain Microcircuits. Oxford Univ. Press; 2010. p. 148-164.
8. Freund TF, Antal M. GABA-containing neurons in the septum control inhibitory interneurons in the hippocampus. Nature. 1988; 336:170–173. [PubMed: 3185735]
9. Mizuseki K, Sirota A, Pastalkova E, Buzsáki G. Theta oscillations provide temporal windows for local circuit computation in the entorhinal-hippocampal loop. Neuron. 2009; 64:267–280. [PubMed: 19874793]
10. Szentágothai J, Arbib MA. Conceptual models of neural organization. Neurosci. Res. Program Bull. 1974; 12:305–510. [PubMed: 4437759]
11. Somogyi P. A specific 'axo-axonal' interneuron in the visual cortex of the rat. Brain Res. 1977; 136:345–350. [PubMed: 922488]
12. Klausberger T, et al. Brain-state- and cell-type-specific firing of hippocampal interneurons *in vivo*. Nature. 2003; 421:844–848. [PubMed: 12594513]
13. Klausberger T, et al. Spike timing of dendrite-targeting bistratified cells during hippocampal network oscillations *in vivo*. Nat. Neurosci. 2004; 7:41–47. [PubMed: 14634650]
14. Gulyás AI, Miles R, Hajos N, Freund TF. Precision and variability in postsynaptic target selection of inhibitory cells in the hippocampal CA3 region. Eur. J. Neurosci. 1993; 5:1729–1751. [PubMed: 8124523]
15. Ishizuka N, Cowan WM, Amaral DG. A quantitative analysis of the dendritic organization of pyramidal cells in the rat hippocampus. J. Comp. Neurol. 1995; 362:17–45. [PubMed: 8576427]

16. Fisahn A, Neddens J, Yan L, Buonanno A. Neuregulin-1 modulates hippocampal gamma oscillations: implications for schizophrenia. Cereb. Cortex. 2009; 19:612–618. [PubMed: 18632742]
17. Sugita S, Ho A, Sudhof TC. NECABs: a family of neuronal Ca^{2+}-binding proteins with an unusual domain structure and a restricted expression pattern. Neuroscience. 2002; 112:51–63. [PubMed: 12044471]
18. Jenkins SM, Bennett V. Ankyrin-G coordinates assembly of the spectrin-based membrane skeleton, voltage-gated sodium channels, and L1 CAMs at Purkinje neuron initial segments. J. Cell Biol. 2001; 155:739–746. [PubMed: 11724816]
19. Kosaka T. The axon initial segment as a synaptic site—ultrastructure and synaptology of the initial segment of the pyramidal cell in the rat hippocampus (CA3 region). J. Neurocytol. 1980; 9:861–882. [PubMed: 7205337]
20. Lapray D, et al. Behavior-dependent specialization of identified hippocampal interneurons. Nat. Neurosci. 2012; 15:1265–1271. [PubMed: 22864613]
21. Dugladze T, Schmitz D, Whittington MA, Vida I, Gloveli T. Segregation of axonal and somatic activity during fast network oscillations. Science. 2012; 336:1458–1461. [PubMed: 22700932]
22. Tukker JJ, Fuentealba P, Hartwich K, Somogyi P, Klausberger T. Cell type-specific tuning of hippocampal interneuron firing during gamma oscillations *in vivo*. J. Neurosci. 2007; 27:8184–8189. [PubMed: 17670965]
23. Lasztóczi B, Tukker JJ, Somogyi P, Klausberger T. Terminal field and firing selectivity of cholecystokinin-expressing interneurons in the hippocampal CA3 area. J. Neurosci. 2011; 31:18073–18093. [PubMed: 22159120]
24. Tukker JJ, et al. Distinct dendritic arborization and *in vivo* firing patterns of parvalbumin-expressing basket cells in the hippocampal area CA3. J. Neurosci. 2013; 33:6809–6825. [PubMed: 23595740]
25. Richter K, et al. Presynaptic cytomatrix protein Bassoon is localized at both excitatory and inhibitory synapses of rat brain. J. Comp. Neurol. 1999; 408:437–448. [PubMed: 10340516]
26. Dávid C, Schleicher A, Zuschratter W, Staiger JF. The innervation of parvalbumin-containing interneurons by VIP-immunopositive interneurons in the primary somatosensory cortex of the adult rat. Eur. J. Neurosci. 2007; 25:2329–2340. [PubMed: 17445231]
27. Acsády L, Kamondi A, Sik A, Freund T, Buzsáki G. GABAergic cells are the major postsynaptic targets of mossy fibers in the rat hippocampus. J. Neurosci. 1998; 18:3386–3403. [PubMed: 9547246]
28. Shigemoto R, et al. Differential presynaptic localization of metabotropic glutamate receptor subtypes in the rat hippocampus. J. Neurosci. 1997; 17:7503–7522. [PubMed: 9295396]
29. Szabadics J, Varga C, Brunner J, Chen K, Soltesz I. Granule cells in the CA3 area. J. Neurosci. 2010; 30:8296–8307. [PubMed: 20554881]
30. Huang Y, et al. Distribution of Satb1 in the central nervous system of adult mice. Neurosci. Res. 2011; 71:12–21. [PubMed: 21658419]
31. Baude A, Bleasdale C, Dalezios Y, Somogyi P, Klausberger T. Immunoreactivity for the $GABA_A$ receptor alpha1 subunit, somatostatin and Connexin36 distinguishes axoaxonic, basket, and bistratified interneurons of the rat hippocampus. Cereb. Cortex. 2007; 17:2094–2107. [PubMed: 17122364]
32. Varga C, Golshani P, Soltesz I. Frequency-invariant temporal ordering of interneuronal discharges during hippocampal oscillations in awake mice. Proc. Natl. Acad. Sci. USA. 2012; 109:E2726–E2734. [PubMed: 23010933]
33. Swanson LW, Cowan WM. The connections of the septal region in the rat. J. Comp. Neurol. 1979; 186:621–655. [PubMed: 15116692]
34. Nielsen JV, Blom JB, Noraberg J, Jensen NA. Zbtb20-induced CA1 pyramidal neuron development and area enlargement in the cerebral midline cortex of mice. Cereb. Cortex. 2010; 20:1904–1914. [PubMed: 19955470]
35. Freund TF. GABAergic septohippocampal neurons contain parvalbumin. Brain Res. 1989; 478:375–381. [PubMed: 2924136]

36. Chaudhry FA, et al. The vesicular GABA transporter, VGAT, localizes to synaptic vesicles in sets of glycinergic as well as GABAergic neurons. J. Neurosci. 1998; 18:9733–9750. [PubMed: 9822734]
37. Fritschy J-M, Harvey RJ, Schwarz G. Gephyrin: where do we stand, where do we go? Trends Neurosci. 2008; 31:257–264. [PubMed: 18403029]
38. Varga V, et al. The presence of pacemaker HCN channels identifies theta rhythmic GABAergic neurons in the medial septum. J. Physiol. 2008; 586:3893–3915. (Lond.). [PubMed: 18565991]
39. Borhegyi Z, Varga V, Szilagyi N, Fabo D, Freund TF. Phase segregation of medial septal GABAergic neurons during hippocampal theta activity. J. Neurosci. 2004; 24:8470–8479. [PubMed: 15456820]
40. Dragoi G, Carpi D, Recce M, Csicsvari J, Buzsáki G. Interactions between hippocampus and medial septum during sharp waves and theta oscillation in the behaving rat. J. Neurosci. 1999; 19:6191–6199. [PubMed: 10407055]
41. Zhang L, et al. Hippocampal theta-driving cells revealed by Granger causality. Hippocampus. 2012; 22:1781–1793. [PubMed: 22416017]
42. Papp OI, Karlócai MR, Tóth IE, Freund TF, Hájos N. Different input and output properties characterize parvalbumin-positive basket and axo-axonic cells in the hippocampal CA3 subfield. Hippocampus. 2013; 23:903–918. [PubMed: 23733415]
43. Miles R. Synaptic excitation of inhibitory cells by single CA3 hippocampal pyramidal cells of the guinea-pig in vitro. J. Physiol. 1990; 428:61–77. (Lond.). [PubMed: 2231426]
44. Wilson MA, McNaughton BL. Reactivation of hippocampal ensemble memories during sleep. Science. 1994; 265:676–679. [PubMed: 8036517]
45. Szabadics J, et al. Excitatory effect of GABAergic axo-axonic cells in cortical microcircuits. Science. 2006; 311:233–235. [PubMed: 16410524]
46. Woodruff AR, et al. State-dependent function of neocortical chandelier cells. J. Neurosci. 2011; 31:17872–17886. [PubMed: 22159102]
47. Glickfeld L, Roberts J, Somogyi P, Scanziani M. Interneurons hyperpolarize pyramidal cells along their entire somatodendritic axis. Nat. Neurosci. 2009; 12:21–23. [PubMed: 19029887]
48. Gulyás AI, et al. Parvalbumin-containing fast-spiking basket cells generate the field potential oscillations induced by cholinergic receptor activation in the hippocampus. J. Neurosci. 2010; 30:15134–15145. [PubMed: 21068319]
49. Denaxa M, et al. Maturation-promoting activity of SATB1 in MGE-derived cortical interneurons. Cell Rep. 2012; 2:1351–1362. [PubMed: 23142661]
50. Close J, et al. Satb1 is an activity-modulated transcription factor required for the terminal differentiation and connectivity of medial ganglionic eminence-derived cortical interneurons. J. Neurosci. 2012; 32:17690–17705. [PubMed: 23223290]
51. Pinault D. A novel single-cell staining procedure performed *in vivo* under electrophysiological control: morpho-functional features of juxtacellularly labeled thalamic cells and other central neurons with biocytin or neurobiotin. J. Neurosci. Methods. 1996; 65:113–136. [PubMed: 8740589]
52. Gerfen CR, Sawchenko P. An anterograde neuroanatomical tracing method that shows the detailed morphology of neurons, their axons and terminals: immunohistochemical localization of an axonally transported plant lectin, *Phaseolus vulgaris* leucoagglutinin (PHA-L). Brain Res. 1984; 290:219–238. [PubMed: 6198041]
53. Sloviter RS. Calcium-binding protein (calbindin-D28k) and parvalbumin immunocytochemistry: localization in the rat hippocampus with specific reference to the selective vulnerability of hippocampal neurons to seizure activity. J. Comp. Neurol. 1989; 280:183–196. [PubMed: 2925892]

Europe PMC Funders Author Manuscripts

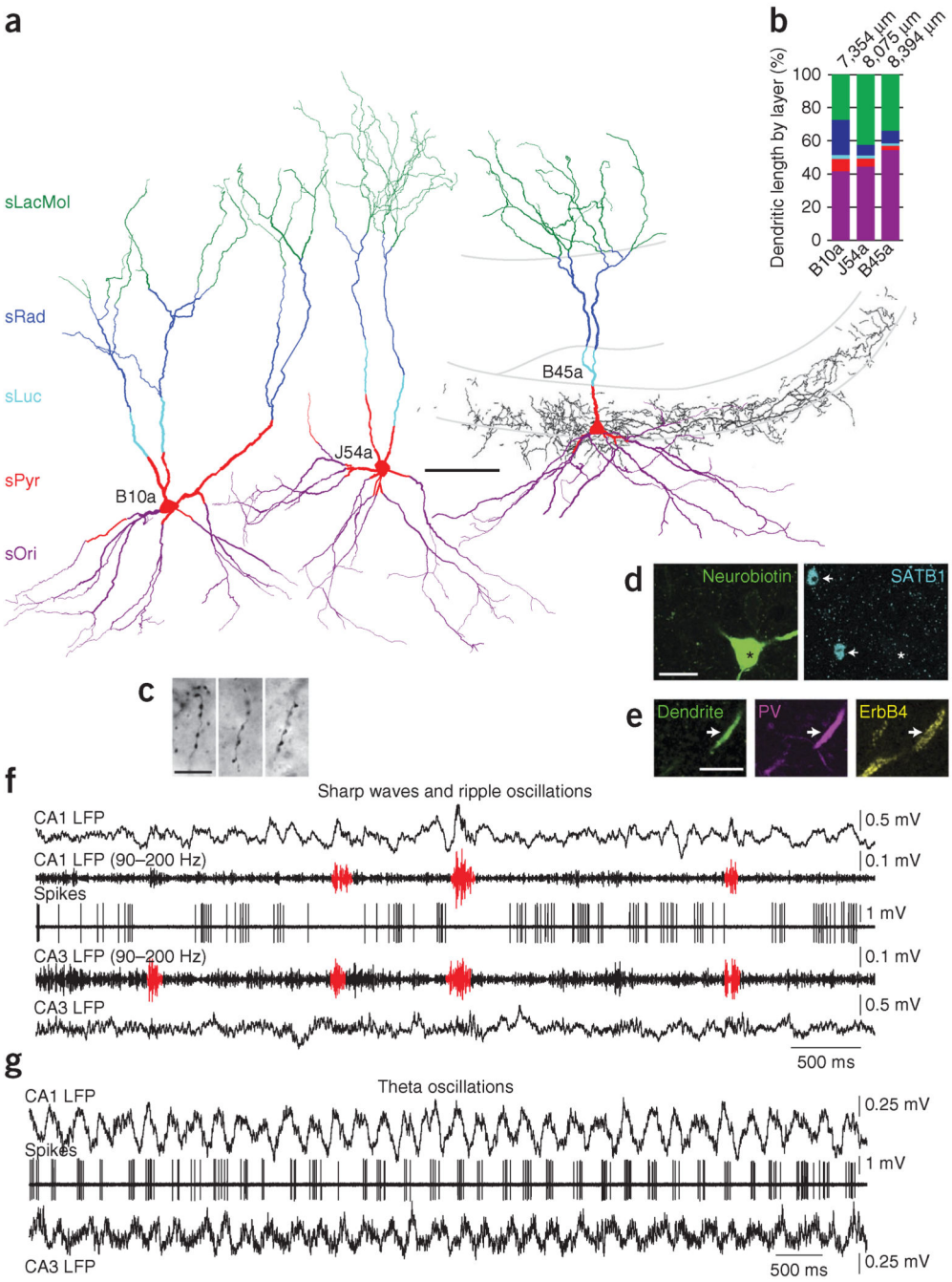

Figure 1.

Identified CA3 AACs fire less during SWR events *in vivo*. (**a**) Full reconstruction of somata and dendrites of three identified AACs (cells B10a, J54a and B45a, from 11, 9 and 11 70-µm-thick sections of rats B10, J54 and B45, respectively), color-coded for layers (sOri includes alveus). The axon of B45a (black) is shown from one section. (**b**) Distribution of dendritic lengths, with total length shown at top. (**c**) Light microscopic images of B45a axon cartridges, identifying the cell type. (**d**) Somatic neurobiotin labeling of B45a (left, asterisk) and SATB1 immunoreactivity (blue, right) in the nuclei of two unidentified cells (arrows);

the AAC is immunonegative (asterisk). (**e**) A neurobiotin-labeled proximal dendrite of B45a (left, arrow) is immunopositive for parvalbumin (PV) and ErbB4. (**f,g**) Firing patterns of cell B45a during SWRs (**f**) and theta oscillations (**g**). Top to bottom in **f**: LFP recorded in CA1 sPyr, first unprocessed and then band-pass filtered at 90–200 Hz; action potentials of the cell (spikes); LFP simultaneously recorded by a tetrode in sPyr of CA3b-c, first band-pass filtered and then unprocessed. Detected ripples are shown in red. Firing of the cell is suppressed during SWRs in CA3 and CA1. Top to bottom in **g**: CA1 LFP; spikes; CA3 LFP from the tetrode. The cell fires rhythmically at the peak of CA1 theta oscillations. Theta oscillations in CA3 are coherent with those in CA1. Scale bars (μm): **a**, 100; **c,e**, 10; **d**, 20. Panel **e**, maximum intensity projection of 13 optical sections (5.1-μm-thick *z*-stack); **d**, two 0.33-μm-thick optical sections from two different depths in the same *z*-stack.

Europe PMC Funders Author Manuscripts

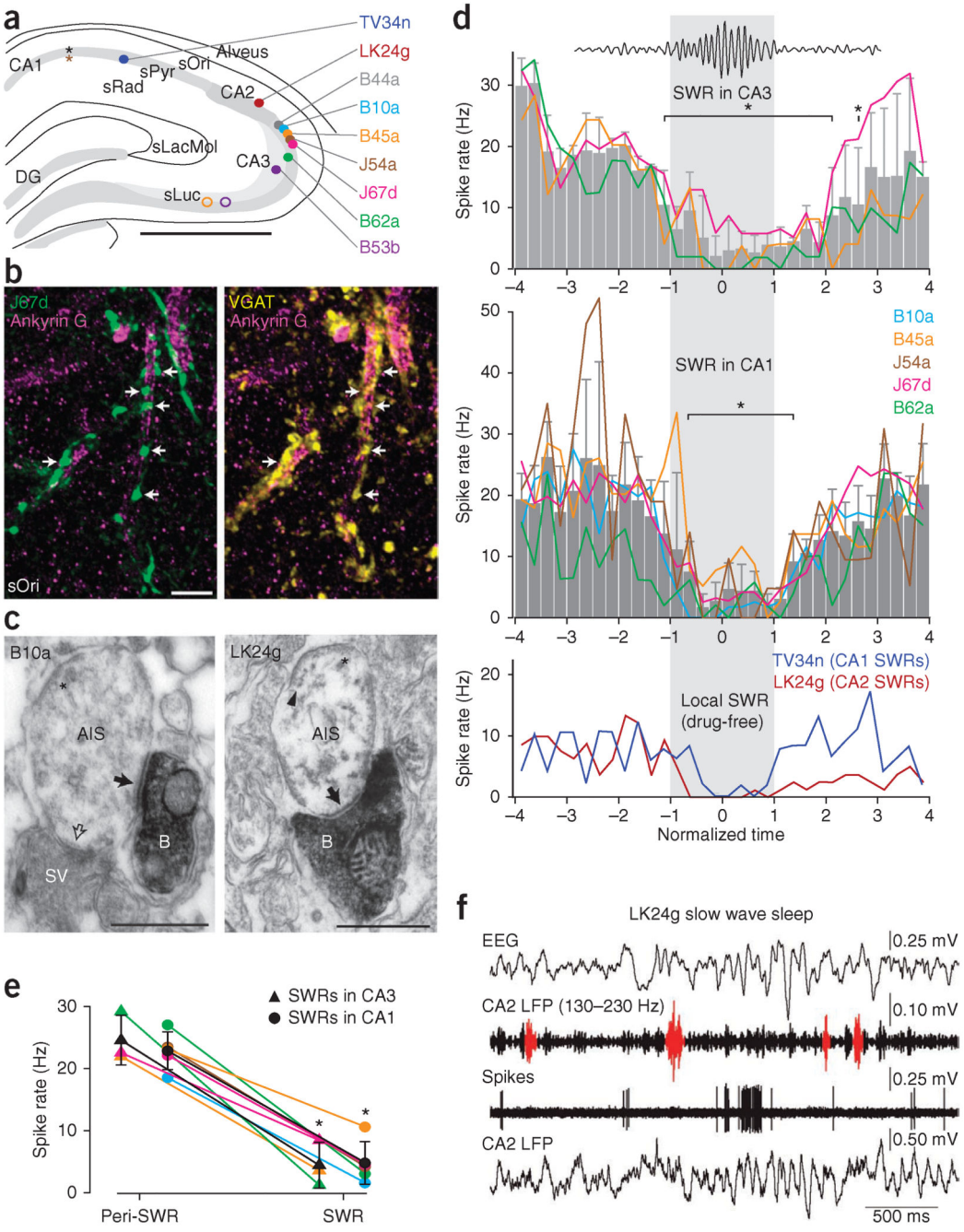

Figure 2.

GABAergic input to CA3 pyramidal cell AISs is withdrawn during sharp waves *in vivo*. (**a**) Locations of CA1 electrodes (black asterisk, rats B44, B10, B45, J67, B62 and B53; brown asterisk, rat J54), tetrode tips (color-coded open circles) and somata of AACs (color-coded filled circles). TV34n and LK24g are from drug-free, freely moving rats. (**b,c**) Examples of AACs (**b**, J67d; **c**, B10a and LK24g) innervating pyramidal cell AISs. (**b**) Neurobiotin-filled axonal boutons (green, arrows), immunoreactive for VGAT (yellow, right) are apposed to AISs immunolabeled for ankyrin G (magenta). (**c**) Electron micrographs of neurobiotin-

Europe PMC Funders Author Manuscripts

labeled (horseradish peroxidase end product) boutons (B) of B10a (left) and LK24g (right) making type II synapses (filled arrows) with AISs, identified by membrane undercoating (asterisk) and linked microtubules (arrowhead). An unlabeled bouton also makes a synapse (open arrow). SV, synaptic vesicles. (**d**) Variation of firing rate of AACs before, during (gray box) and after SWRs detected in CA3 (top) or CA1 (middle; lines, individual cells; gray bars, mean ± s.d.; asterisks significant at $\alpha = 0.05$ by Tukey's *post hoc* comparisons). Bottom: firing rates for identified AACs TV34n and LK24g recorded in drug-free rats; SWRs detected from the electrode recording the cell. (**e**) Overall firing rates during and outside SWRs (peri-SWR) detected in CA3 or CA1. Individual cells are color-coded as in **a** (mean ± s.d. in black; asterisks, significant at $\alpha = 0.05$ with paired *t*-test; $P = 0.039$ and 6×10^{-4} for SWRs detected in CA3 and CA1, respectively). (**f**) Firing of LK24g during sleep. Top to bottom traces: Electroencephalogram (EEG) in frontal cortex; band-pass filtered (130–230 Hz) LFP at the recording site of the cell (CA2), SWRs in red; action potentials; LFP. Scale bars: **a**, 1 mm; **b**, 5 μm; **c**, 0.5 μm. Panel **b**, maximum intensity projection of 9 optical sections (2.8-μm-thick *z*-stack). DG, dentate gyrus.

Europe PMC Funders Author Manuscripts

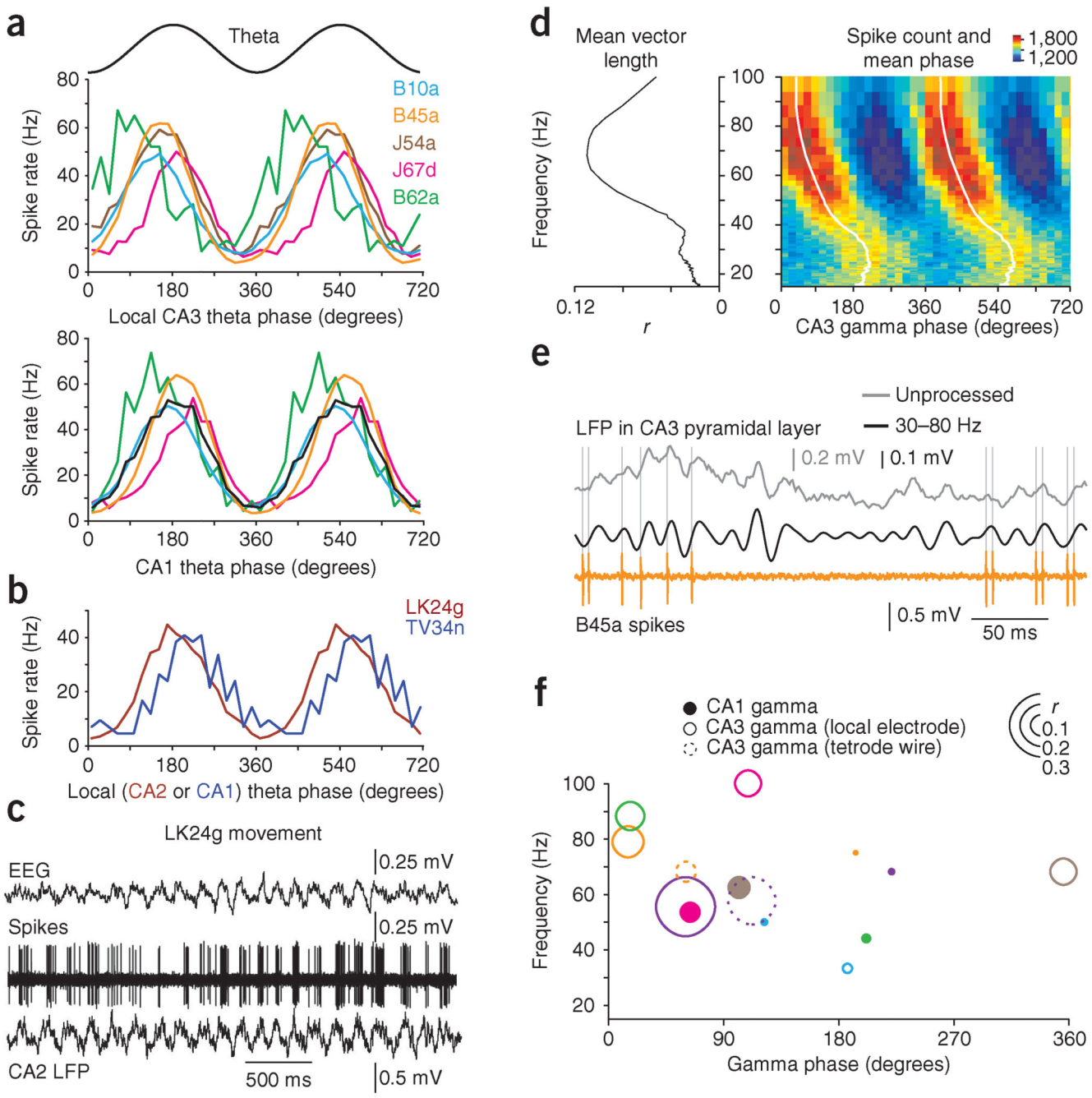

Figure 3.

AACs in CA3 fire rhythmically around the peak of theta oscillations and are coupled to gamma oscillations *in vivo*. (**a**) Firing rate of AACs (color-coded) as a function of theta phase (sinusoid shown above) recorded locally in CA3 (top) and at a reference site in CA1 (bottom; black trace is the mean). (**b**) Firing rate versus theta phase (local electrode) for identified AACs recorded from drug-free rats in CA2 (LK24g) and CA1 (TV34n). (**c**) Firing patterns of LK24g during head movement of the rat. Top to bottom traces: electroencephalogram (EEG); action potentials of the cell; LFP revealing rhythmic theta

oscillations. (**d**) Modulation of spike timing (cell B45a) by the phase of gamma oscillations from a CA3 tetrode. Left, mean vector length (*r*) as a function of gamma frequency (15–100 Hz, 85 logarithmically equidistant bins). Right, spike count (color-coded) binned as a function of gamma phase (20 bins per cycle) and frequency (15–100 Hz, 85 logarithmically equidistant bins). White line, mean phase spectrum. (**e**) Representative LFP and spikes for the same cell as in **d**. Unprocessed CA3 tetrode LFP (gray), filtered tetrode LFP (gamma, 30–80 Hz, black), spikes (orange). (**f**) Summary of gamma coupling for all cells recorded in anesthetized rats (color code as in **a**; B53b, purple). Position of circle represents the frequency at which the coupling is maximal and the mean phase observed at this frequency. Size of circle represents coupling strength (vector length, *r*) at the same frequency. Filled, open and dashed circles represent AAC coupling to gamma oscillations recorded by CA1 electrode, local CA3 electrode and a tetrode wire in CA3, respectively (for positions, consult Fig. 2a).

Europe PMC Funders Author Manuscripts

Europe PMC Funders Author Manuscripts

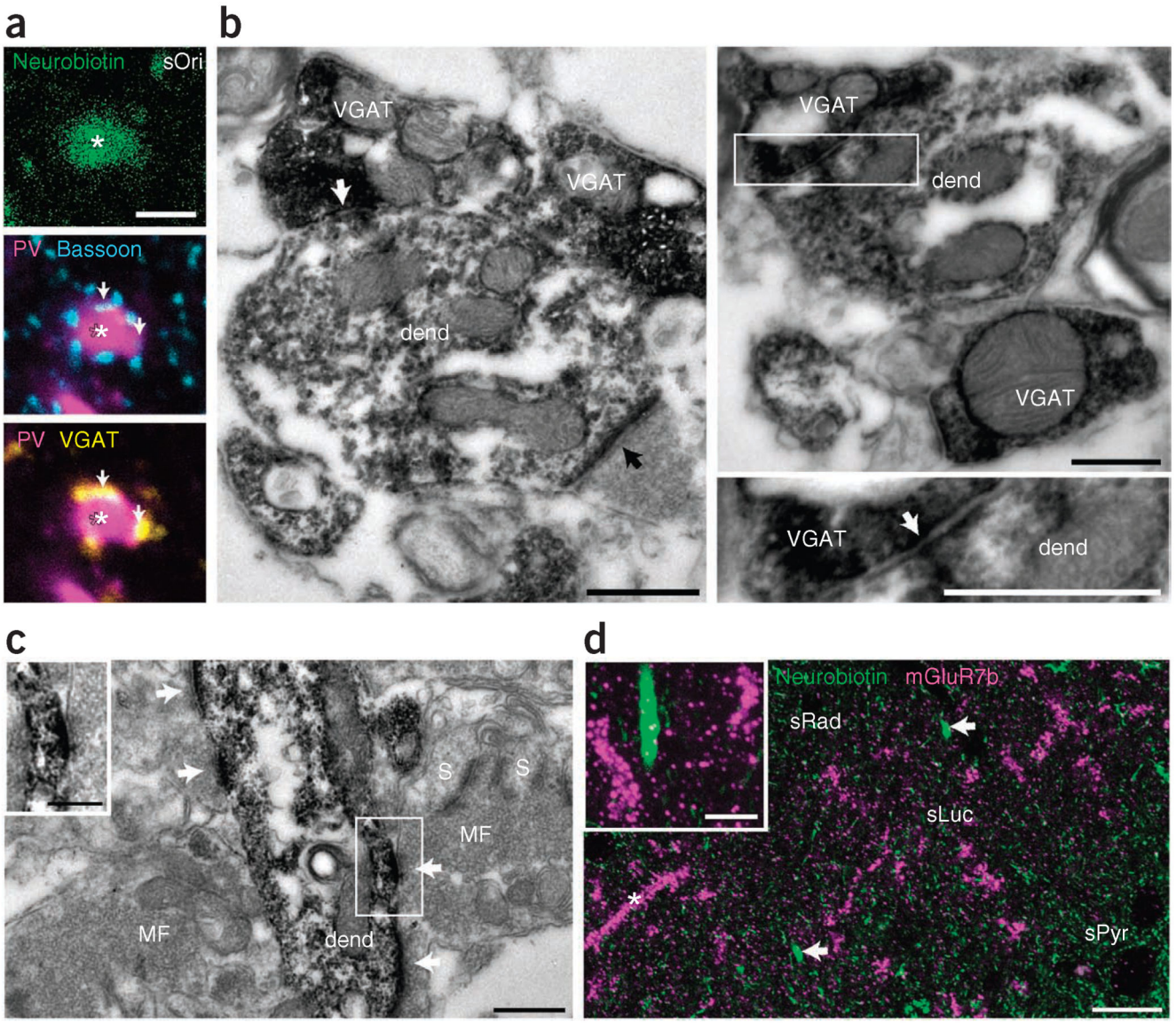

Figure 4.

Innervation of AAC dendrites by GABAergic and mossy fiber terminals. (**a**) Synaptic input to an AAC dendrite (asterisk, cell B10a, single optical section) in sOri. Neurobiotin, green; parvalbumin, magenta; bassoon, cyan; VGAT, yellow. A subset of bassoon puncta apposed to the dendrite colocalize VGAT (arrows). (**b**) Electron micrographs of $VGAT^{+}$ terminals (containing Ni^{2+}-intensified electron-opaque reaction product of horseradish peroxidase) making type II synapses (white arrows; boxed region on right enlarged below) and a VGAT-negative bouton (black arrow) making a type I synapse with a neurobiotin-labeled AAC dendrite (dend, horseradish peroxidase reaction product, B10a, two cross-sections at different levels). (**c**) Electron micrograph of a neurobiotin-labeled AAC dendrite (dend, B10a) receiving synaptic input (white arrows) from three small boutons, and a large mossy fiber bouton (MF) recognized by dense vesicular filling. S, thorny excrescence of CA3 pyramidal cell dendrite. (**d**) Confocal maximum intensity projection (13 optical sections,

4.29-μm-thick *z*-stack) of mGluR7b immunoreactivity in presynaptic terminals (magenta) and AAC dendrites (arrows; neurobiotin, green; J54a). Asterisk, unlabeled strongly mGluR7b-decorated dendrite. Small green dots, mitochondrial endogenous biotin. Inset, single optical section demonstrating lack of mGluR7b puncta apposed to the labeled AAC dendrite. Two unlabeled mGluR7b-decorated dendrites are on either side. Scale bars (μm): **a**, 2; **b**, 0.5; **c**, 0.5, inset 0.25; **d**, 20, inset 5.

Europe PMC Funders Author Manuscripts

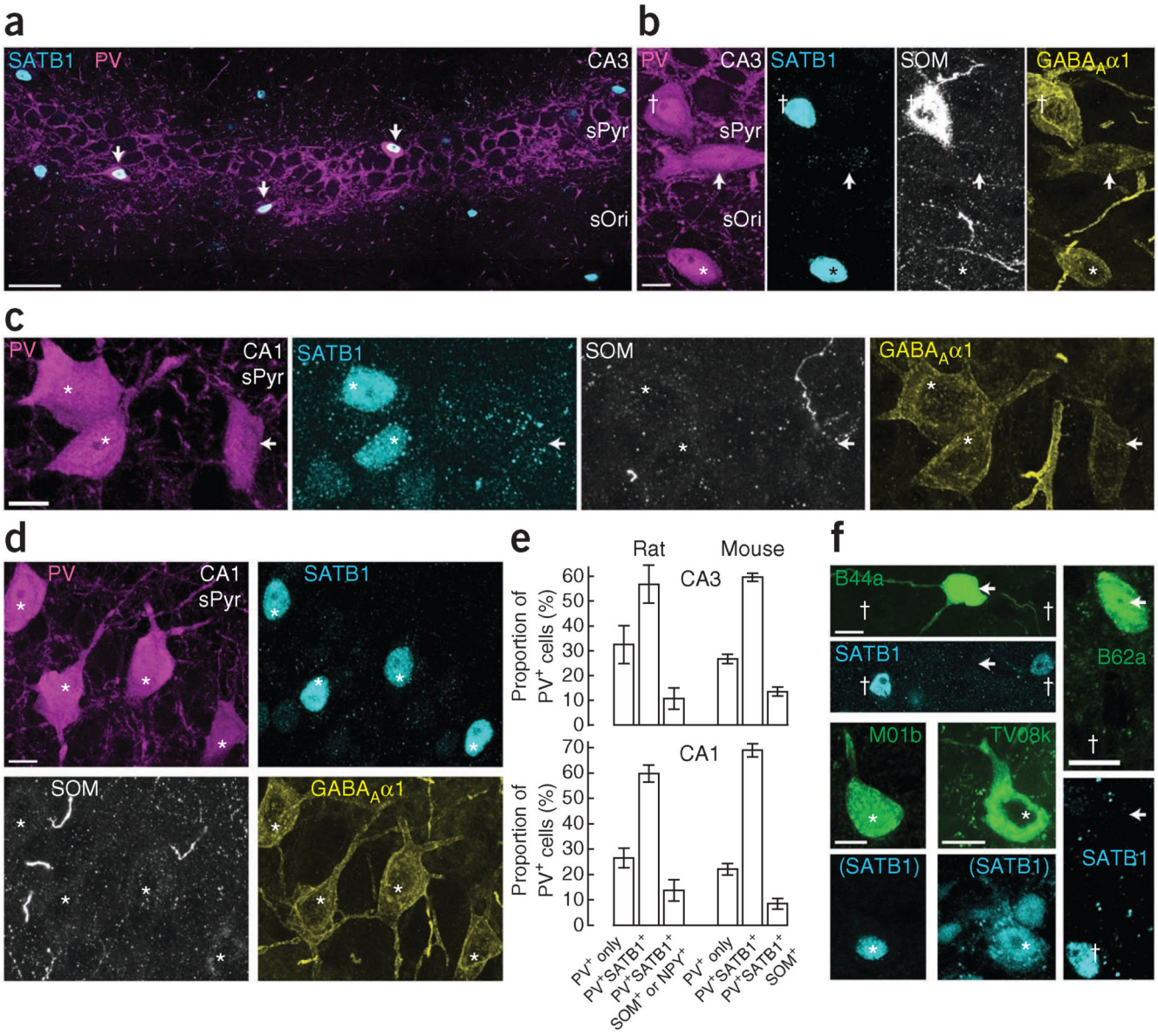

Figure 5.

AACs are SATB1-immunonegative, PV$^+$ interneurons. (**a**) SATB1 (cyan, nuclei) and parvalbumin (magenta) immunoreactivity in a single-optical-section montage of CA3; three PV$^+$ somata in sPyr show nuclear SATB1 immunoreactivity (arrows). (**b**) Three CA3 PV$^+$ neurons (left, magenta) show differential immunoreactivity for SATB1 and SOM (middle panels, cyan and white); neurons are SATB1$^+$ (nucleus, dagger) and SOM$^+$, or immunonegative for both (arrow), or immunoreactive only for SATB1 (asterisk). All three neurons show immunoreactivity for the α1 subunit of the GABA$_A$ receptor (right, yellow). (**c**) Three CA1 PV$^+$ neurons (magenta); two of them are SATB1$^+$ (cyan, asterisks), one is SATB1$^-$ (arrow). All lack immunoreactivity for SOM (white) but are immunopositive for GABA$_A\alpha$1 (yellow). In **b,c**, note the weak GABA$_A\alpha$1 immunoreactivity of the SATB1$^-$ cell. (**d**) A cluster of four CA1 PV$^+$SATB1$^+$GABA$_A\alpha$1$^+$SOM$^-$ neurons (asterisks). (**e**)

Quantification of rat and mouse PV^+ neurons in sPyr of CA3 (top) and CA1 (bottom), mean ± s.e.m., $n = 4$ areas in each species. (**f**) Neurobiotin-labeled, identified PV^+ interneurons (green) and SATB1 immunoreactivity (cyan). Two *in vivo*–recorded CA3 AACs, B44a and B62a, are immunonegative for SATB1 (arrows), but nearby unrecorded neurons (daggers) are immunopositive. Two neurobiotin-labeled CA1 PVBCs, TV08k[20] and M01b, are $SATB1^+$ (asterisks). SATB1 in parentheses indicates mouse anti-SATB2 antibody, which recognizes both SATB2 and SATB1 (Supplementary Table 2). Confocal *z*-stack maximum intensity projections; number of optical sections (thickness in μm): **b**, 12 (5.4); **c**, 15 (6.75); **d**, 16 (7.2). Scale bars (μm): **a**, 50; **b–d,f**, 10.

Europe PMC Funders Author Manuscripts

Europe PMC Funders Author Manuscripts

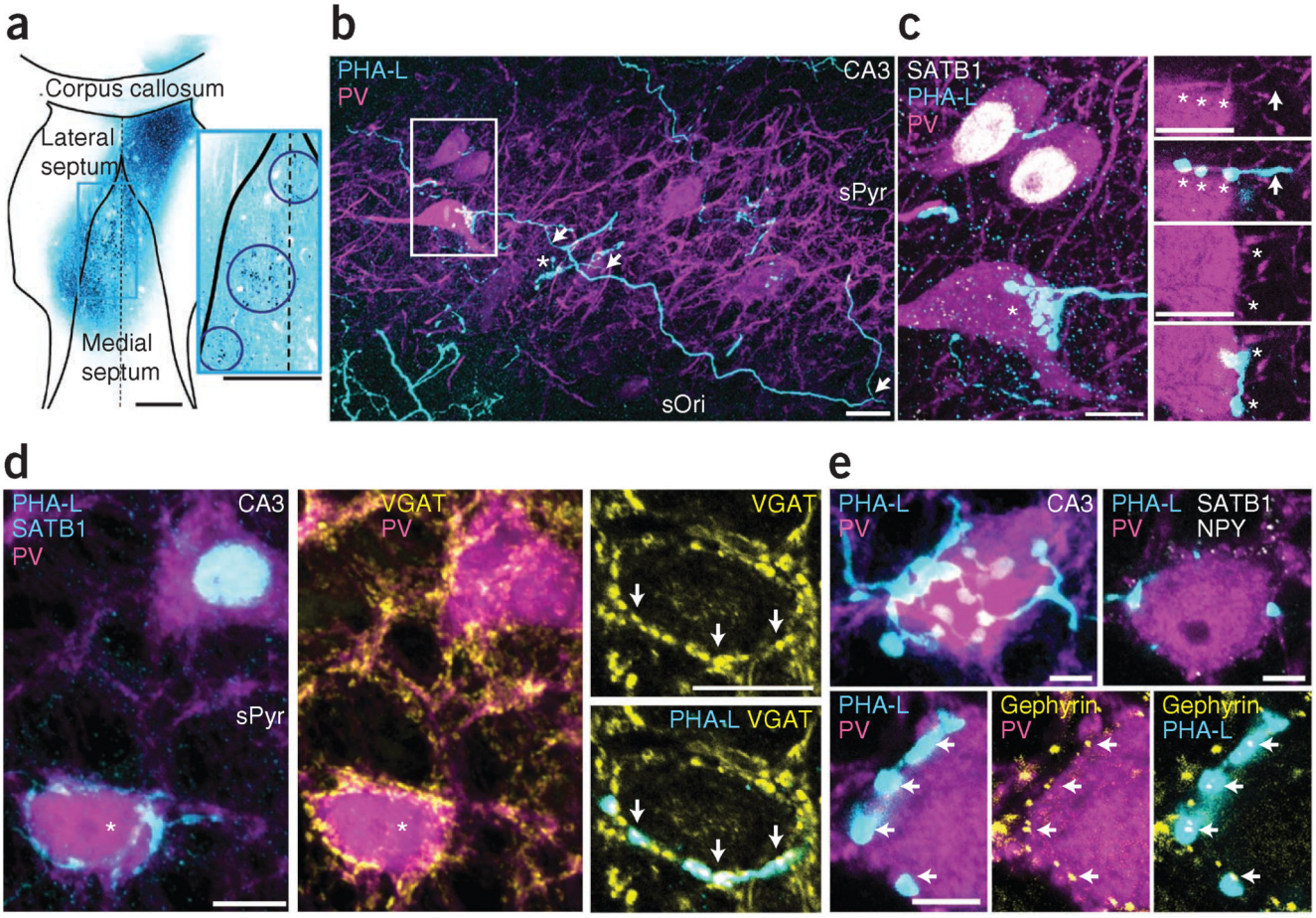

Figure 6.

A preferential medial septal GABAergic input to the somata of AACs identified by SATB1^{-}PV^{+} labeling in CA3. (**a**) PHA-L injection sites in medial septum (cyan, single-optical-section 10× objective montage). Inset, enlargement of boxed region showing three injection sites (circled). Dashed line, midline. (**b**) PHA-L^{+} septo-hippocampal axons (cyan) contact PV^{+} neurons (magenta). The axon (arrows) emits three collaterals; one ends in boutons targeting a PV^{+} soma (box), another targets an unlabeled cell (asterisk). (**c**) Left (from box in **b**), two of three PV^{+} somata (magenta) are SATB1^{+} (white, nuclei); the third is SATB1^{-} and receives septal innervation from the labeled axon (asterisk). Right, two single optical sections (from the *z*-stack at left) show septal boutons (asterisks) with undetectable immunoreactivity for parvalbumin apposed to the SATB1^{-}PV^{+} soma. Axon, arrow. (**d**) Left, one SATB1^{-}PV^{+} cell (asterisk) receives PHA-L^{+} innervation (cyan); another SATB1^{+} (cyan nucleus) cell is not innervated. Middle, both somata are surrounded by VGAT^{+} puncta (yellow). Right, single optical section of the SATB1^{-} cell (asterisk, left image), showing VGAT^{+}PHA-L^{+} septal boutons (arrows). (**e**) Top left, dense septal innervation (cyan) of a PV^{+} soma (magenta). Top right, single optical section with additional immunoreactions for SATB1 and NPY (both white), both undetectable in the cell (see Supplementary Fig. 5d,e). Bottom, single optical section; PHA-L^{+} boutons on PV^{+} soma colocalize gephyrin puncta (yellow, arrows) but lack detectable parvalbumin immunoreactivity. Confocal *z*-stacks,

number of optical sections (thickness in μm)/intensity projection mode: **b**, 124 (62)/ maximum (tile); **c** left, 40 (14)/average; **d**, 50 (16)/average; **e** top left, 68 (21)/average. Scale bars (μm): **a**, both 500; **b**, 20; **c,d**, 10; **e**, 5.

Europe PMC Funders Author Manuscripts

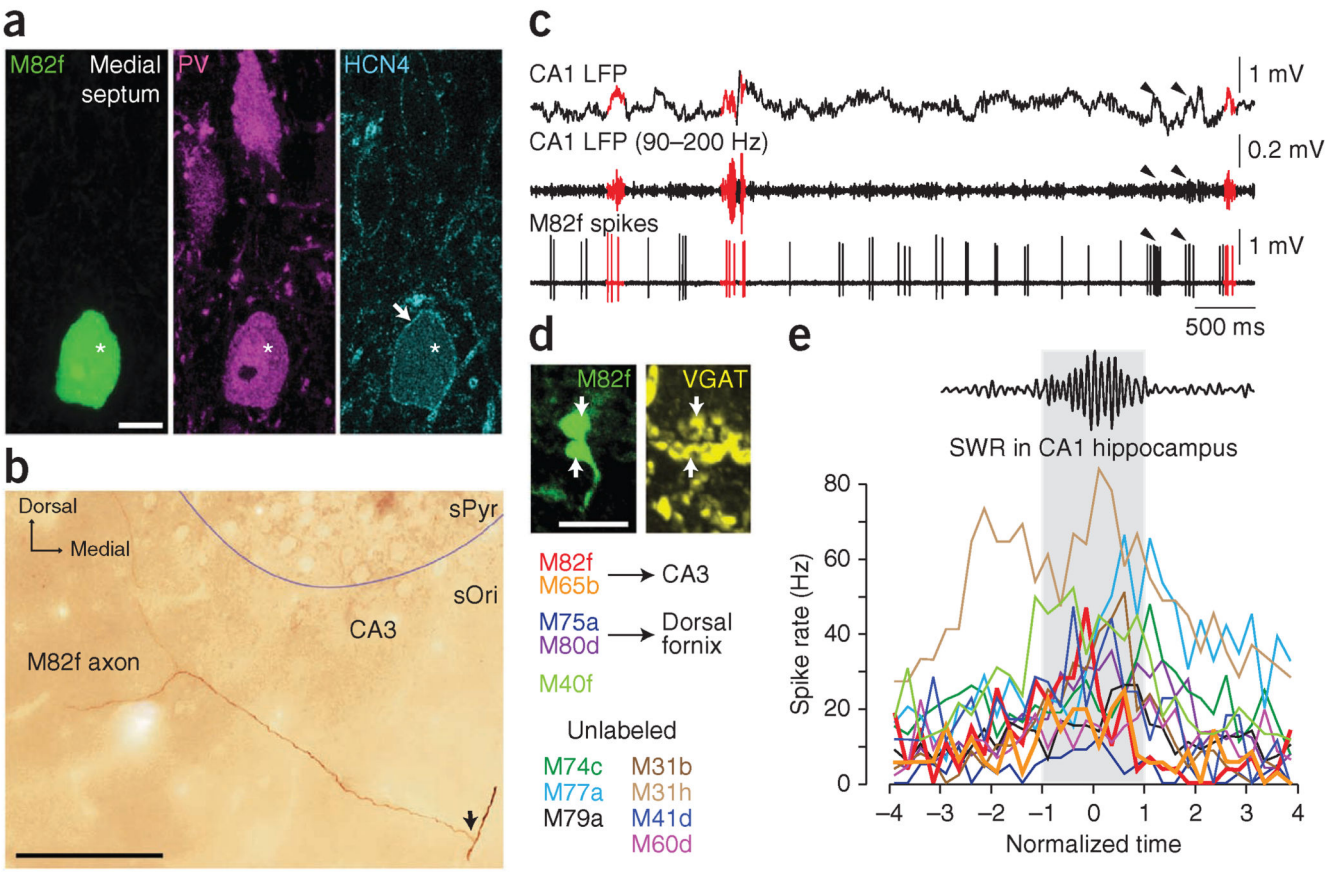

Figure 7.

A subset of GABAergic medial septal cells increase their firing during sharp waves *in vivo* and project to CA3. (**a**) Identified septo-hippocampal GABAergic neuron M82f recorded *in vivo* and shown in a single optical section (soma, neurobiotin, green, left; asterisk). The cell is immunoreactive for parvalbumin (magenta, middle) and HCN4 (cyan, right; arrow, plasma membrane). (**b**) The main axon of M82f in the fimbria of the hippocampus (arrow) branches into CA3 (photographic *z* reconstruction). (**c**) Some firing patterns of M82f (bottom trace) are associated with the occurrence of SWRs recorded in CA1 (LFP and ripple-filtered LFP in top traces, SWRs plotted in red, arrowheads point to events below the threshold for ripple detection). Note rhythmic firing. (**d**) VGAT-immunoreactive axon boutons (arrows) of M82f in the medial septum (confocal maximum intensity projection *z*-stack from 7 optical sections, 2.6 μm thick). (**e**) Sharp wave–associated firing rate variation of medial septal cells that fired significantly (at $\alpha = 0.05$; Mann Whitney *U*-test) more during SWRs than during peri-SWR periods. Gray area designates the time of SWRs (normalized). Cells are color-coded (left) and those identified with axons projecting to CA3 are shown with thick lines. Scale bars (μm): **a**, 10; **b**, 100; **d**, 5.

Europe PMC Funders Author Manuscripts

Table 1

Properties of identified AACs

Cell Region	B44a[a] CA3	B10a CA3	B45a CA3	J54a[b] CA3	J67d CA3	B62a CA3	B53b[c] CA3	LK24g[d] CA2	TV34n[d,e] CA1
Immunohistochemistry, histology									
Parvalbumin	+ D	+ D	+ D	+ D	+ D	+ A	+ DS	+ D	+ A
SATB1	− N		− N		− N	− N	− N	− N	
ErbB4	+ D		+ D		+ D	+ DS	+ DS		
NECAB 1	− D		− D		− D		− D		
Somatostatin			− S		− S				
Neuropeptide Y	− S					− S			
VGAT	+ A				+ A		+ A		
GABAergic input (VGAT)		+ D		+ D	+ D				
Calbindin			− D		− AD				
Targets AIS (ankyrin G)	+ A				+ A		+ A		
Targets AIS (EM)	+ (10/10)	+ (7/7)	+ (14/14)				+ (9/9)	+ (13/13)	+ (11/11)
***In vivo* firing patterns**									
CA2/3 SWRs									
Rate during SWRs (Hz)	NA	NA	3.5	NA	8.4	1.2	NA	0.7	NA
Rate peri-SWR (Hz)	NA	NA	21.9	NA	22.5	29.2	NA	8.8	NA
U-test *P* value	NA	NA	2×10^{-6}	NA	10^{-10}	5×10^{-19}	NA	6×10^{-7}	NA
Total *n* SWRs (active *n*)	NA	NA	23 (4)	NA	80 (28)	50 (3)	NA	112 (5)	NA
CA1 SWRs									
Rate during SWRs (Hz)	NA	1.5	10.6	4.1	4.5	3.0	2.6	NA	2.4
Rate peri-SWR (Hz)	NA	18.5	23.1	23.5	22.1	27	8.3	NA	6.9
U-test *P* value	NA	4×10^{-32}	5×10^{-5}	3×10^{-6}	6×10^{-31}	10^{-13}	0.250	NA	0.026
Total *n* SWRs (active *n*)	NA	106 (11)	28 (12)	20 (6)	147 (35)	49 (7)	7 (1)	NA	61 (7)
Non-theta firing rate (Hz)	NA	19.4[f]	NR	NR	19.7[f]	27.9	7.63		
Theta firing rate (Hz)	NA	25.9	29.0	32.1	23.5	33.4	3.2	20.4	17.5
Head movement rate (Hz)								17.1	24.4
Slow-wave sleep rate (Hz)								8.2	6.0
Quiet wakefulness rate (Hz)								7.2	8.8
Theta coupling									
Mean phase CA2/3 (°)	NA	142.2	152.7	153.6	193.4	94.8	138.4	190.6	NA
Mean vector length CA2/3	NA	0.39	0.51	0.38	0.44	0.38	0.54	0.48	NA
Rayleigh test *P* value	NA	$<10^{-100}$	$<10^{-100}$	$<10^{-100}$	$<10^{-100}$	10^{-29}	3×10^{-7}	$<10^{-100}$	NA
Mean phase CA1 (°)	NA	169.7	194.9	247.3	218.4	154.4	178.7	NA	225.3
Mean vector length CA1	NA	0.43	0.54	0.36	0.43	0.45	0.51	NA	0.42
Rayleigh test *P* value	NA	$<10^{-100}$	$<10^{-100}$	$<10^{-100}$	$<10^{-100}$	7×10^{-21}	4×10^{-8}	NA	6×10^{-14}
Total *n* spikes	NA	19,195	20,706	3,880	1,691	308	54	1,897	164

Positive and negative immunoreactivity or connectivity indicated by + and −, respectively. Measurement location: S, soma; N, nucleus; D, dendrites; A, axons; NA, not available; NR, not recorded. EM, electron microscopic evidence. *U*-test (Mann-Whitney *U* comparison) *P* values

significantly different from peri-SWR at $\alpha = 0.05$. Rayleigh test P values significantly different from a uniform phase distribution of spikes at $\alpha = 0.05$.

[a] The recorded firing patterns could not be assigned to a cell because two labeled cells were recovered.

[b] CA1 electrode LFP recorded in sRad, accounting for a CA1 theta phase shift.

[c] Cell recorded under unusually deep anesthesia.

[d] Recorded in drug-free freely moving rats.

[e] The soma and dendrites were lost during labeling.

[f] Significantly different from the theta firing rate (Mann-Whitney U-test at $\alpha = 0.05$).

Europe PMC Funders Author Manuscripts